DIFFRACTIVE INTERACTIONS OF HADRONS AT HIGH ENERGIES

K. GOULIANOS

The Rockefeller University, New York, NY 10021, U.S.A.

Contents:

Abstract:

Hadronic elastic scattering, inclusive diffraction dissociation and total cross sections are reviewed, with emphasis on phenomenological descriptions of experimental results.

DIFFRACTIVE INTERACTIONS OF HADRONS AT HIGH ENERGIES

K. GOULIANOS

The Rockefeller University, New York, NY 10021, U.S.A.

1. Introduction

Experiments at Fermilab, at the SPS and at the ISR over the last decade have unveiled some very simple universal features of elastic scattering, of diffraction dissociation and of the total cross section of hadrons at high energies. Examples are the similarity, among hadrons, of the shrinking of the forward elastic scattering peak with increasing energy, of the $1/M_x^2$ behavior of diffraction dissociation and of the rising of the total cross sections at high energies. Below $s \sim 200 \text{ GeV}^2$, these simple features are masked by contributions from terms which fall as inverse powers of s. As the energy increases, the novel characteristics of diffraction become clearly identifiable. This is illustrated in figs. 1, 2 and 3 for elastic scattering [1], for diffraction dissociation [2], and for the total cross sections [3], respectively. The total cross section is, of course, not entirely a diffractive process. However, since it is intimately related to elastic scattering through the optical theorem and dispersion relations, and to diffraction dissociation through factorization rules, we find it necessary to include it in our discussion of diffractive processes.

Figure 1 shows the differential cross section, $d\sigma/dt$, for pp elastic scattering. As the energy increases, the forward elastic peak becomes visibly exponential and a secondary diffraction maximum appears. The exponential behavior at small t is reminiscent of the diffraction of light by a circular aperture. The intensity of the scattered light as a function of angle is given by

$$\frac{I}{I_0} = \frac{[2J_1(x)]^2}{x} \cong 1 - \frac{R^2}{4}(k\theta)^2 \tag{1}$$

where k is the wave number of the photons, R is the radius of the aperture and $x = kR \sin \theta \cong kR\theta$. For pp elastic scattering

$$\frac{d\sigma/dt}{(d\sigma/dt)_{t=0}} = e^{bt} \cong 1 - b\,(p\theta)^2 \tag{2}$$

where p is the momentum of the incident proton. Comparison of eqs. (1) and (2) leads to a relationship between the radius of interaction and the slope parameter:

$$b = R^2/4 . \tag{3}$$

For $R = 1/m_\pi$, which is the typical radius of strong interactions, eq. (3) yields $b = 12.5 \text{ (GeV}/c)^{-2}$. This is well within the range of the measured slope parameter values for pp elastic scattering at high energies (see fig. 10a). Thus, as in the diffraction of light, the slope of the forward elastic peak reflects the size of the scattering object.

Figure 2 shows the invariant differential cross section $d^2\sigma/dt\, d(M_x^2/s)$ as a function of M_x^2/s for the diffraction dissociation of protons on hydrogen, $pp \rightarrow Xp$, at $t = -0.042 \text{ (GeV}/c)^2$ and s from 13 to 500 GeV^2. For $|t| \ll M_x^2$, which is the case here, M_x^2/s is related to the Feynman scaling variable $x = p/p_{\parallel,\text{max}}$ by the equation

$$\frac{M_x^2 - M_p^2}{s} \cong 1 - x . \tag{4}$$

The phenomenological significance of this variable is that the quantity $M_p(1 - x)$ represents the forward
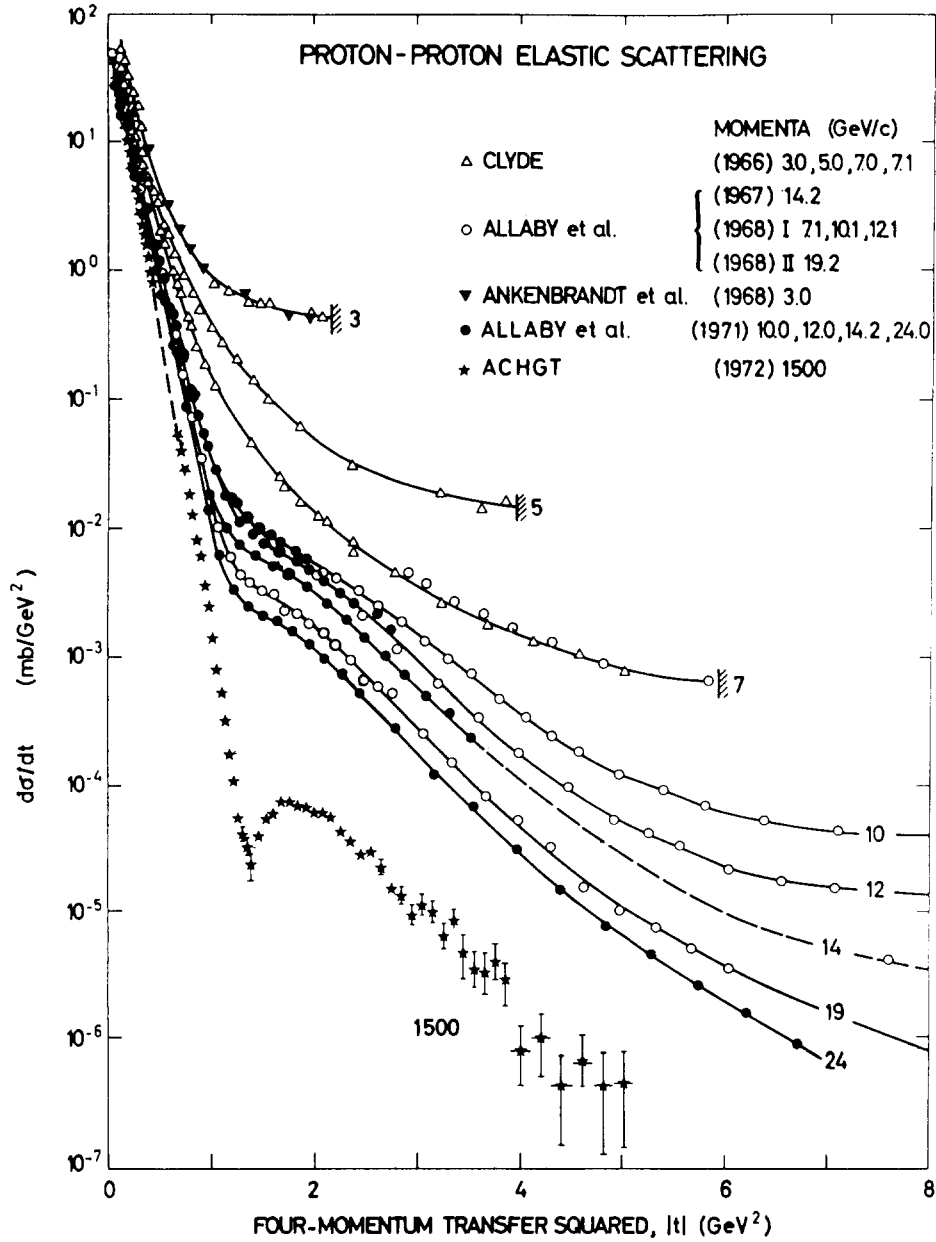
Fig. 1. Proton–proton elastic differential cross section versus four-momentum transfer squared at various incident proton momenta. As the energy increases, a classical diffraction pattern appears to emerge (from ref. [1]).

momentum transfer in the reaction pp → Xp, which is the minimum momentum transfer required for the production of a mass M_x:

$$q_{\parallel} = |t_{min}|^{1/2} = M_p(1 - x) \cong M_p \frac{M_x^2 - M_p^2}{s}. \tag{5}$$

By analogy with optics, diffraction should become increasingly more visible as the wave length
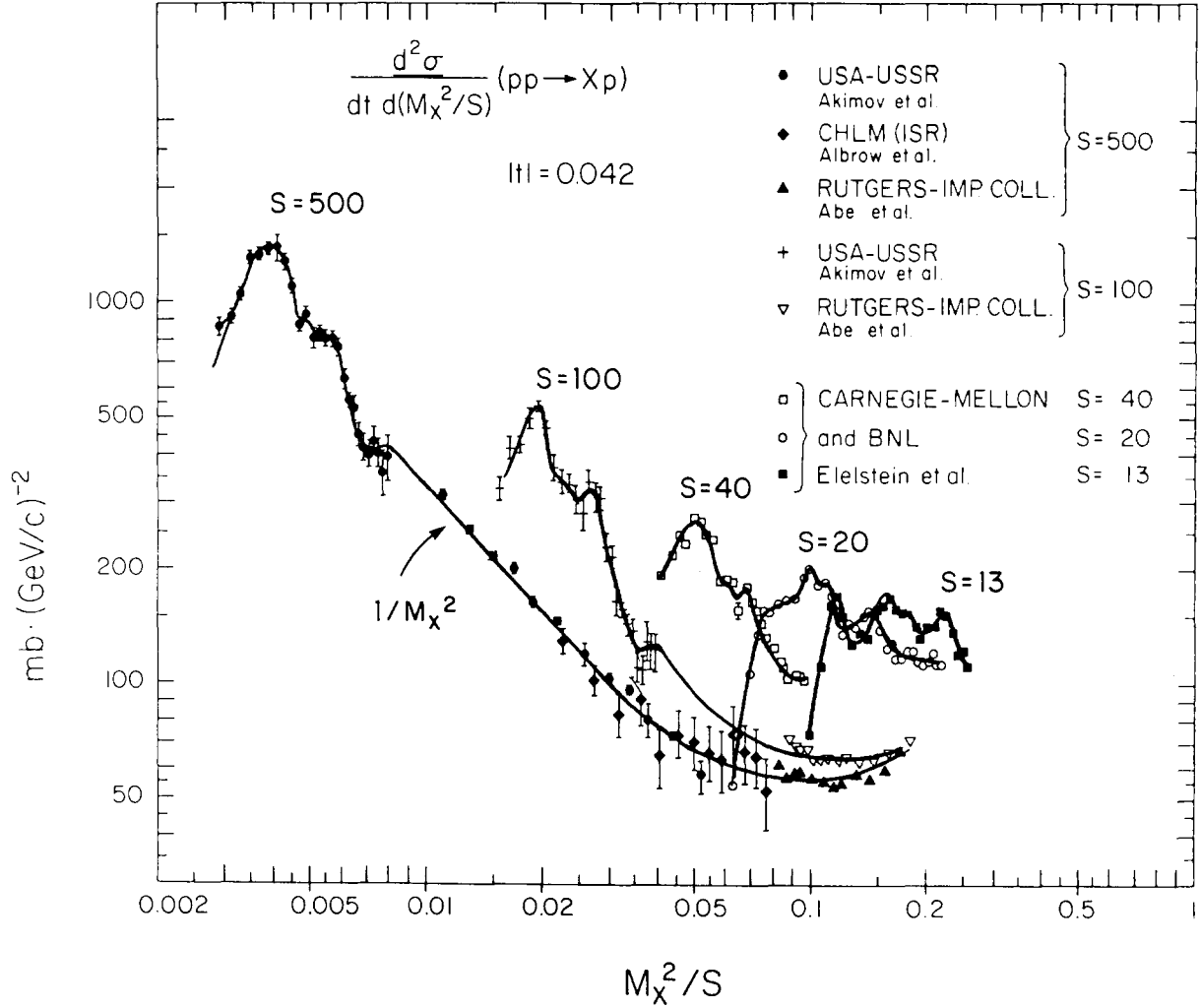
Fig. 2. The invariant differential cross section $d^2\sigma/dt\, d(M_x^2/s)$ for pp→Xp at $t = -0.042\,(GeV/c)^2$, plotted versus M_x^2/s at various values of s (from ref. [2]). As the energy increases, the resonance region moves to smaller values of M_x^2/s while larger masses enter the diffraction region and form a $1/M_x^2$ continuum.

associated with $q_{\parallel}$ becomes larger than the interaction radius. One then expects the condition for observing inelastic diffraction to be

$$1/q_{\parallel} \gtrsim R \tag{6}$$

or, for $R = 1/m_\pi$,

$$1 - x \cong \frac{M_x^2 - M_p^2}{s} \lesssim \frac{m_\pi}{M_p} \cong 0.15 . \tag{7}$$

For a given M_x^2, the higher the s-value, the easier this condition is satisfied. Alternatively, for a given s,

the smaller the value of $1 - x \cong M_x^2/s$, the higher the expected cross section $d\sigma/dx$. These simple ideas find support in experiments at high energies. As seen in fig. 2, the cross section $d\sigma/dx$, which is approximately flat in the central x region (not shown entirely in the figure), increases dramatically with decreasing $1 - x$ in the region $1 - x \lesssim 0.15$. This is the more evident, the higher the s-value. As $1 - x \cong M_x^2/s$ decreases, the value of M_x^2 enters the "resonance region" ($M_x^2 \lesssim 5\,\text{GeV}^2$) and finally reaches the one pion production threshold where the cross section must come down to zero.

Another way of looking at inelastic hadron diffraction, $hp \rightarrow Xp$, is through the idea of coherence. The lower the momentum transfer in the collision, the higher the probability that the target proton will remain intact. In interactions in which the proton does remain intact, there is no exchange of quantum numbers between the incoming hadron and the proton and therefore the hadron is simply excited to a state of higher mass. Since the proton does not change its character, the various amplitudes that originate at different parts of the proton and contribute to this excitation add up coherently. In this picture, coherence is synonymous with diffraction. The condition for coherence is derived from the requirement that the target proton does not emit any pions. Quantitatively, the probability for this is enhanced when $|t|^{1/2} \lesssim m_\pi$ which, through eq. (5), is the same as eq. (7) – the condition for inelastic diffraction arrived at previously. The mass spectra of the diffractively excited states of hadrons generally consist of some resonance-like structures superimposed on a continuum (see fig. 2). These states dissociate with characteristic strong interaction time constants. Resonance production is usually called
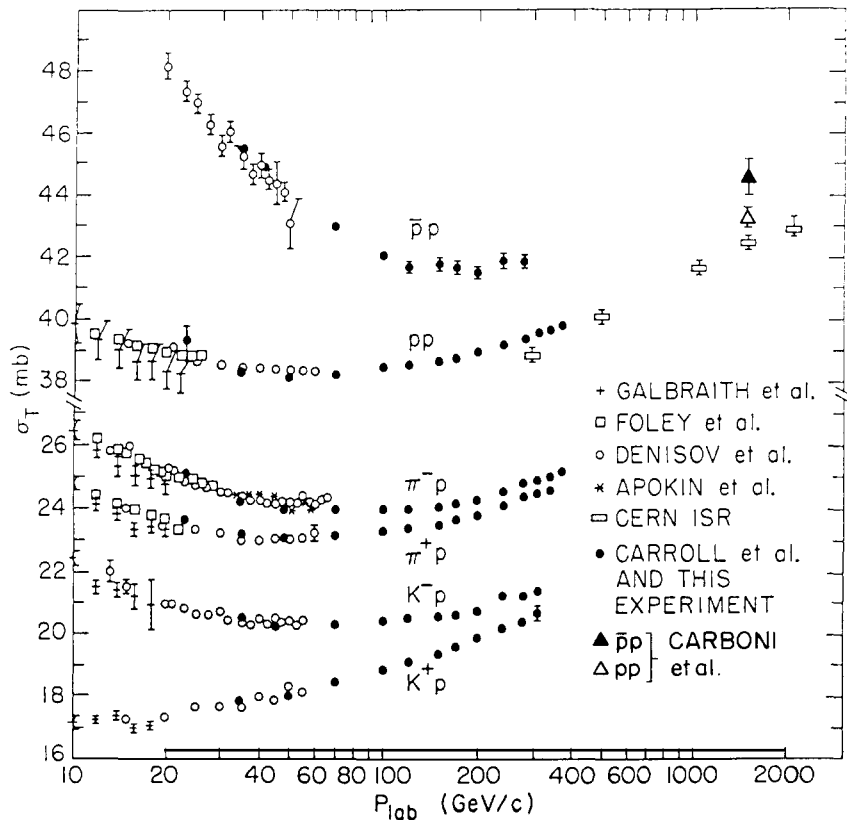

Fig. 3. Total cross sections versus incident hadron momentum for $hp \rightarrow$ anything ($h = p^\pm$, $\pi^\pm$, $K^\pm$). All cross sections exhibit a smooth rise with energy above $\sim 100\,\text{GeV}/c$ (from ref. [3]).

diffractive excitation while the continuum is referred to as diffraction dissociation. However, the two terms are often used interchangeably.

Figure 3 shows the total cross sections of hadrons on protons as a function of energy. Large variations with energy and resonance-like structures that characterize their behavior at low energies (not shown in this figure) fade away as the energy increases. At high energies, all cross sections exhibit a strikingly similar small rise with energy which will be the subject of our discussion in a later section of this report. The question which we will be most interested in addressing is whether this rise can be attributed to contributions from the diffractive processes which also increase with energy.

It is the purpose of this review to elucidate the simple features of diffraction at high energies by following their emergence as the energy increases. In the absence of a theory of low energy diffraction, phenomenological fits are used to provide a continuous transition from the turbulence of low energy behavior to the calmness of high energy asymptopia where theoretical predictions are presently available. Although an effort is made to describe the characteristics of high energy diffraction without any theoretical bias, it will not escape the attention of the reader that most of the observed characteristics are direct predictions [4, 47] of "critical pomeron" $(\alpha(0) = 1)$ Regge-type theories with $\alpha'(0)$ small and $r_0(0) \neq 0$, where $\alpha(t)$ is the pomeron trajector and $r_0(t)$ the triple-pomeron coupling constant. Therefore, anticipating the reader's own conclusion, we will point out, as we describe the various features of the data, the pertinent critical pomeron predictions. However, we will also present empirical fits that serve to organize the data and, therefore, facilitate the testing of other theoretical ideas.

The vast amount of existing data on diffractive interactions of hadrons has been reviewed recently by Alberi and Goggi [4]. In the present report, we focus on elastic scattering and inclusive single diffraction dissociation involving the common hadrons, for it is in these processes that the striking simplicity of the asymptotic high energy behavior has become most apparent. For reasons already mentioned, we also include a discussion of the total cross sections.

Since interpretation of the data involves relationships among parameters discussed at various parts throughout this report, we cannot avoid references to later sections as we proceed with our discussion. For economy of space, and for pedagogical reasons, we present in this introduction an outline of some theoretical ideas which are useful in relating the data. We discuss briefly the optical theorem, dispersion relations, geometrical scaling, factorization, the finite mass sum rule and the Regge phenomenology predictions.

The optical theorem relates the total cross section to the imaginary part of the forward elastic scattering amplitude

$$\text{Im} f(s, 0) = \frac{\sigma_\text{T}(s)}{4\pi} \tag{8}$$

where

$$d\sigma_\text{el}/dt = \pi |f(s, t)|^2 . \tag{9}$$

Dispersion relations provide a connection between the real and the imaginary part of $f(s, t)$ and therefore, in combination with the optical theorem, they relate ρ, the ratio of the real to the imaginary part, to σ_T.

Geometrical scaling [5] assumes that, at high energies, the elastic scattering amplitude in impact

parameter space, l, is purely imaginary and a function of $l/R(s)$ only, where $R(s)$ is the effective interaction radius. The energy dependence is contained entirely in $R(s)$. For spin independent interactions, this hypothesis leads to the expression

$$f(s, t) = i\, R^2(s)\, f[t\, R^2(s)]$$ (10)

from which it follows that

$$\sigma_{el} \sim \sigma_T \sim b \sim R^2(s)$$ (11)

where b is the slope parameter.

The hypothesis of factorization of the diffractive vertex leads to scaling relations among diffraction dissociation, elastic scattering and total cross sections. Figure 4 represents the reactions $h + a \to X + a$ and $h + a \to h + a$. Factorization implies that each amplitude is proportional to the product of the coupling constants $g(t)$ at each vertex. The ratio of diffraction dissociation to elastic scattering is then

$$\frac{d^2\sigma/dt\,dx}{d\sigma_{el}/dt} = \left[\frac{g_{hX}(t)\cdot g_{aa}(t)}{g_{hh}(t)\cdot g_{aa}(t)}\right]^2 = C_h(s, x, t)$$ (12)

i.e., at given s, x and t, the ratio of the diffraction dissociation to the elastic scattering cross section of a hadron h interacting with a target particle a is a constant independent of the target particle. When different hadrons dissociate on the same target, factorization leads to scaling relations only under specific models. For example, if the triple-pomeron amplitude is responsible for diffraction dissociation and simple pomeron exchange for the total cross section (see fig. 5), it follows that

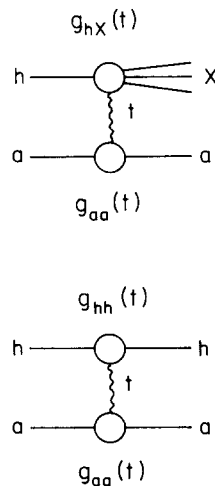$$\frac{d^2\sigma/dt\,dx}{\sigma_T} = C_a(s, x, t)$$ (13)

Fig. 4. Diagrams for the elastic scattering and single diffraction dissociation amplitudes.
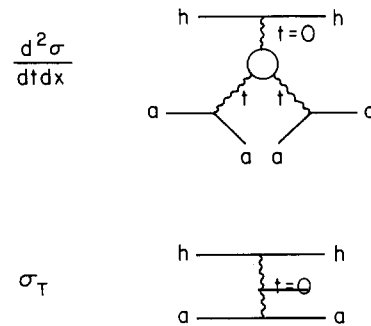
Fig. 5. Pomeron exchange diagrams for the total cross section and for single diffraction dissociation (triple pomeron diagram).

i.e., at given s, x and t, the ratio of the diffraction dissociation to the total cross section of different hadrons h dissociating on the same target particle a is independent of the dissociating hadron.

The finite mass sum rule (FMSR) provides a connection between the high mass and the low mass diffractive cross sections (including elastic scattering). It is an extension of the finite energy sum rule (FESR) which applies to total cross sections. Figure 6 represents the typical behavior of hadronic total cross sections as a function of s. Resonance-like structures, which are prominent at low energies, disappear as the energy increases, and at high energies the cross section becomes a smooth function of s. The low energy region is described best by s-channel resonance production and decay while the high energy behavior is represented well by Reggeon t-channel exchanges. The FESR states that the two descriptions are equivalent so that the extrapolation of the high energy behavior into low energies describes well the average behavior of the cross section in this region. This dual description of the total cross section in terms of s-channel resonance or t-channel Reggeon exchanges is referred to in the literature as duality. A similar description applies to the diffractive cross sections. However, as shown in fig. 7, the relevant variable is now M_x^2 rather than s and therefore one speaks of finite mass rather than finite energy sum rules. The first moment FMSR, which has been derived for triple-Regge amplitudes using analyticity and crossing symmetry [6], states that the extrapolation of the high ν behavior of the function $\nu \, (\mathrm{d}^2\sigma/\mathrm{d}t \, \mathrm{d}\nu)$ into the low ν region, where $\nu = M_x^2 - M_h^2 - t$ is the cross-symmetric variable, represents the average behavior of the resonances (including elastic scattering) in this region (see fig. 7). Quantitatively,

$$|t| \frac{\mathrm{d}\sigma_{el}}{\mathrm{d}t} + \int_0^{\nu_0} \nu \frac{\mathrm{d}^2\sigma}{\mathrm{d}t \, \mathrm{d}\nu} \, \mathrm{d}\nu = \int_0^{\nu_0} \nu \left(\frac{\mathrm{d}^2\sigma}{\mathrm{d}t \, \mathrm{d}\nu}\right)_{\text{fit at high } \nu} \mathrm{d}\nu \tag{14}$$

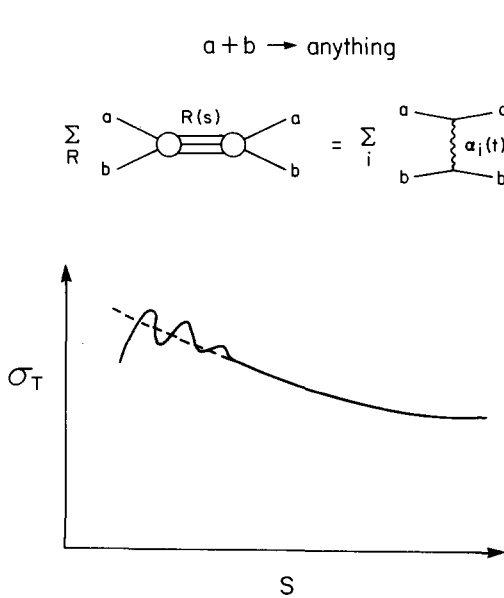Fig. 6. Finite energy sum rule: The extrapolation of the smooth, high s cross section into the low s resonance region represents the average behavior of the cross section in this region.
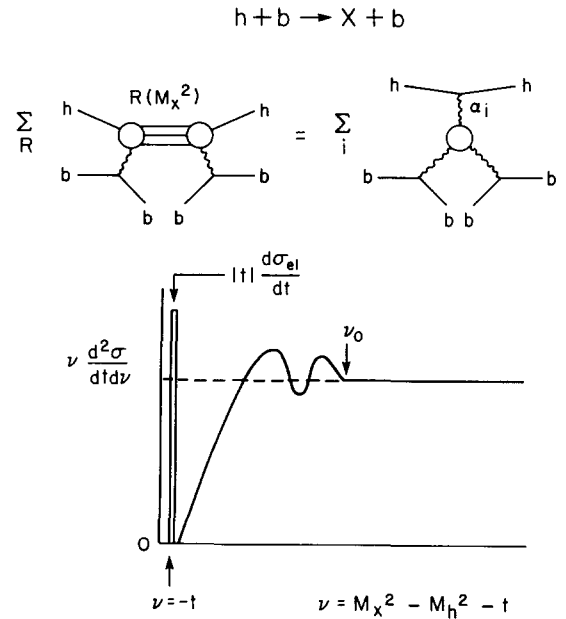
Fig. 7. First moment finite mass sum rule: The extrapolation of $\nu \, \mathrm{d}^2\sigma/\mathrm{d}t \, \mathrm{d}\nu$ from a high ν into the low ν region averages over the resonance-like structures, including elastic scattering.

where the value of ν_0 must lie beyond the "resonance region" but is otherwise arbitrary. This rule has far-reaching consequences which will be discussed in detail in the appropriate sections of this report.

Regge theory provides a framework on the basis of which many features of hadronic diffractive phenomena find a simple explanation. In what follows, we present a brief account of the Regge phenomenology [7] as it applies to the processes of total cross section, elastic scattering and single diffraction dissociation. The Regge diagrams which are shown in fig. 8 are assumed to be solely responsible for these processes. In terms of the Regge trajectories, $\alpha(t)$, and the residue functions, $\beta(t)$, these diagrams lead to the expressions (for s, M_x^2 and $s/M_x^2 \to \infty$)

$$\sigma_T^{ij} = \sum_k \beta_{ik}(0)\,\beta_{ij}(0)\,s^{[\alpha_k(0)-1]} \tag{15}$$

$$\frac{d\sigma_{el}^{ij}}{dt} = \sum_k \frac{\beta_{ik}^2(t)\,\beta_{jk}^2(t)}{16\pi}\,s^{2[\alpha_k(t)-1]} \tag{16}$$

$$s\,\frac{d^2\sigma^{ij}}{dt\,dM_x^2} = \sum_{k,l} \frac{\beta_{ik}(0)\,\beta_{jl}^2(t)\,g_{kll}(t)}{16\pi s}\left(\frac{s}{M_x^2}\right)^{2\alpha_l(t)}(M_x^2)^{\alpha_k(0)}. \tag{17}$$

The most common Regge trajectories are listed below:

Pomeron $\alpha_P(t) = \alpha_P(0) + \alpha_P'(t)\,t$

Reggeon $\alpha_R(t) \cong 0.5 + t$ \tag{18}

Pion $\alpha_\pi(t) \cong 0 + 0.9t$.

As mentioned previously, the available experimental results support the hypothesis that all diffractive processes are dominated by a pomeron trajector with $\alpha_P(0) \cong 1$, $\alpha_P'(0) \lesssim 0.3$ and $g_{PPP}(0) \equiv r_0(0) \neq 0$.
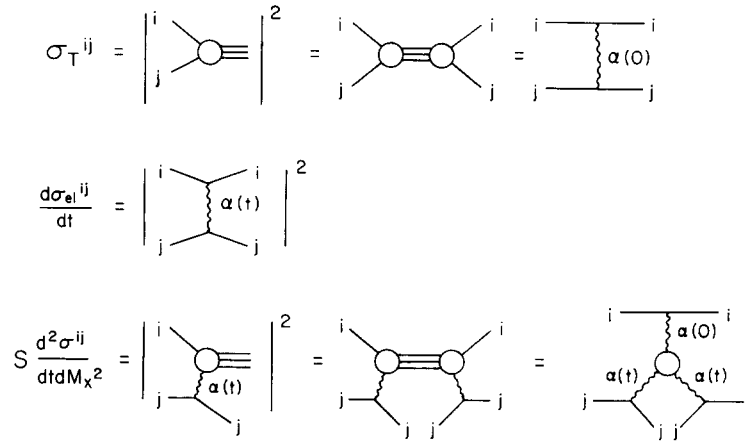

Fig. 8. Regge diagrams for the total cross section, for elastic scattering and for single diffraction dissociation.

Setting $\alpha(t) = 1 + \alpha' t$ in expressions (15), (16) and (17), we obtain

$$\sigma_T^{ij}(s) = \beta_{i\mathbb{P}}(0)\,\beta_{j\mathbb{P}}(0) = \text{constant} \tag{19}$$

$$\frac{\mathrm{d}\sigma_{el}^{ij}(s, t)}{\mathrm{d}t} = \frac{\beta_{i\mathbb{P}}^2(t)\,\beta_{j\mathbb{P}}^2(t)}{16\pi}\, s^{2\alpha'(t)\,t} \tag{20}$$

$$(\text{small } t) = \frac{\sigma_T^2}{16\pi}\, e^{b(s,t)\,t}\,; \qquad b(s, t) = b_0(t) + 2\alpha'(t)\ln s$$

$$\frac{\mathrm{d}^2\sigma^{ij}(s, M_x^2, t)}{\mathrm{d}t\,\mathrm{d}M_x^2} = \frac{\beta_{i\mathbb{P}}(0)\,\beta_{j\mathbb{P}}^2(t)\,g_{\mathbb{PPP}}(t)}{16\pi M_x^2}\left(\frac{s}{M_x^2}\right)^{2\alpha'(t)\,t} \tag{21}$$

$$(\text{small } t) = \frac{A}{M_x^2}\, e^{b_D(s,t)\,t}\,; \qquad b_D(s, t) = b_{D,0}(t) + 2\alpha'(t)\ln\frac{s}{M_x^2}$$

where, in the last lines of eqs. (20) and (21), we used for the t-dependence at small t the familiar parametrization e^{bt}. Thus, under pomeron dominance and for the simple diagrams of fig. 8, the total cross sections are constant with energy, the forward elastic and diffraction dissociation peaks shrink logarithmically with s, and the diffraction dissociation cross sections are independent of s and vary as $1/M_x^2$. Also, implicit in eqs. (19), (20) and (21) are the factorization properties discussed previously. The shrinking of the diffractive peak is universal in that it depends on $\alpha_\mathbb{P}'(t)$ and not on the hadrons involved in the process. In critical pomeron Reggeon field theories, where all other diagrams in addition to those in fig. 8 are taken into account, these results are modified slightly. For example, the total cross sections are constant only up to logarithms of s which cause a slow rise with energy. A full account of these results is given in various review papers [4, 50].

2. Elastic scattering

Elastic scattering is closer to classical diffraction than any other particle process. The angular or t distribution obtained in the collision of two hadrons (see fig. 1) is strikingly similar to the diffraction pattern resulting from the passage of light through a small aperture or the scattering of light by a small black disc. The shape and size of this pattern reflect the wave nature of the colliding particles and the range of their interaction.

From an experimental as well as a theoretical point of view, it is convenient to divide elastic scattering into two regions: the small angle or low t region, which is dominated by the diffraction peak, and the large angle or high t region, which is characterized by a diffraction minimum and a secondary diffraction maximum. A complete theory should, of course, predict t distributions for the entire t region over which cross sections vary by more than ten orders of magnitude. The critical pomeron Reggeon field theory offers such a prediction only in the limit $s \to \infty$. Phenomenological models usually apply either to the low t or to the high t region. They are nevertheless useful in that they serve to organize and relate the data, particularly at low energies where the predictions for asymptotic behavior are not valid.

2.1. Low t elastic scattering

At small momentum transfer, $|t| \lesssim 0.3\,(\text{GeV}/c)^2$, the differential cross section for elastic scattering, $h + p \to h + p$, is described well by the expression

$$d\sigma_{el}/dt = \pi |f_N + f_C|^2 \tag{22}$$

where the nuclear and Coulomb scattering amplitudes have the forms

$$f_N = \frac{\sigma_T}{4\pi}(\rho + i)\,e^{b/2\,t} \tag{23}$$

$$f_C = -\frac{2\alpha}{t}\,G_h(t)\,G_p(t)\,e^{i\alpha\phi} \,. \tag{24}$$

The real and imaginary parts of the nuclear scattering amplitude are assumed to have the same t-dependence and spin effects are neglected. The slope parameter b is a slowly varying function of both s and t. In the expression for f_C, α is the fine structure constant and $G(t)$ are charge form factors whose dipole forms are given by

$$G_h(t) = 1/(1 + \nu_h|t|)^2 \tag{25}$$

where the parameters ν_h are related to the electromagnetic radii of the hadrons: $\nu_h = r_h^2/12$. For protons,
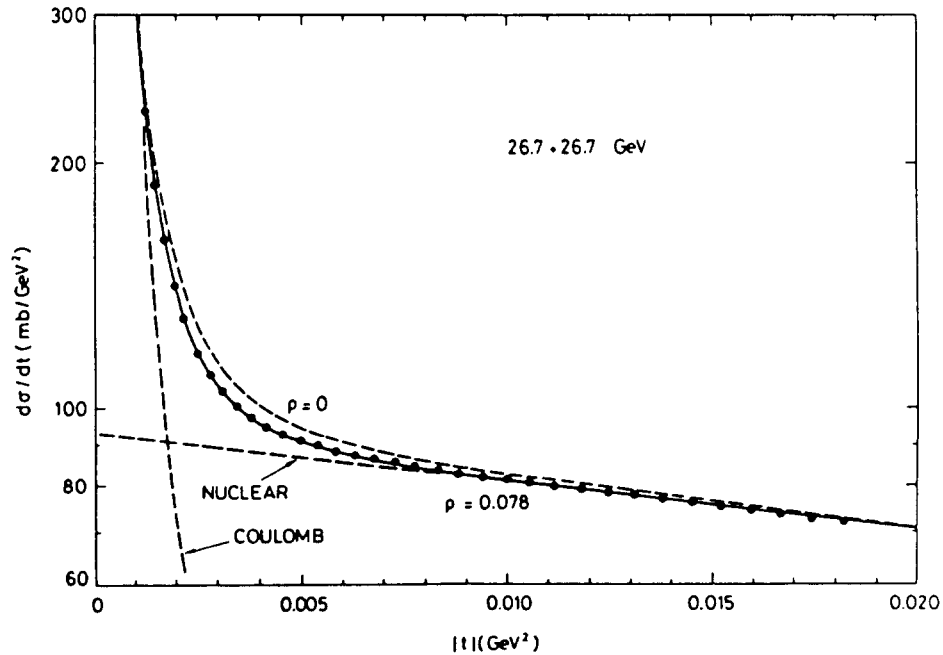

Fig. 9. Small t pp elastic differential cross section at $\sqrt{s} = 53.4\,\text{GeV}$ [10]. The full line is a fit to the data using formula (22). The Coulomb and nuclear contributions are also shown separately.

pions and kaons $r = 0.805$, 0.711 and 0.566 fm, respectively [8], so that $\nu_h \sim 1\,(\mathrm{GeV}/c)^{-2}$. The phase of the Coulomb amplitude, $\alpha\phi$, is given by [9]

$$\alpha\phi = \alpha\,\ln[1.124/((b(0) + 4\nu_p + 4\nu_h)|t|)]\,. \tag{26}$$

This angle is small, so that the Coulomb amplitude is mostly real. The ρ-value is determined from the interference of the Coulomb with the nuclear amplitude. The interference term is maximum when the two amplitudes are comparable in magnitude. This occurs at $|t| \cong 8\pi\alpha/\sigma_T$ which for $\sigma_T = 36$ mb is $0.002\,(\mathrm{GeV}/c)^2$. Figure 9 shows the differential cross section for pp elastic scattering at low t [10]. The Coulomb, the nuclear and the interference regions are clearly identifiable. The parameters b and ρ are obtained from fits to the differential cross section using the formulae described above.

2.1.1. The slope parameter of the forward nuclear scattering amplitude

The slope parameter b is a slowly varying function of both s and t. Regge phenomenology predicts an explicit form for the s-dependence of b at high energies,

$$b(s, t) = b_0(t) + 2\alpha'(t)\ln s \tag{27}$$

while geometrical scaling relates it to that of σ_T:

$$b(s) \sim \sigma_T(s)\,. \tag{28}$$

Neither model predicts the t-dependence.

Since the s-dependence in the Regge picture is controlled by the slope of the pomeron trajectory, the shrinking of the forward peak with energy is expected to be universal; i.e., the same for all hadrons. This is not necessarily the case in the geometrical scaling picture, unless the rise of the total cross sections with energy is itself universal. The term "high energies", where predictions (27) and (28) are expected to be valid, is not well defined theoretically. However, it is reasonable to assume that the energy is high enough when the total cross sections have started rising smoothly and the ρ-values have become small. This happens above $\sqrt{s} \sim 15$ GeV (see figs. 3 and 16). At lower energies, the cross sections contain terms which fall as inverse powers of s and which are responsible for the larger ρ-values. As these terms die out and diffraction becomes the dominant process, the features that are expected to characterize the asymptotic behavior start to appear.

Figure 10a shows b as a function of s for pp scattering [11]. Above ~ 100 GeV, the increase of b with energy follows that of the total cross section as expected by the geometrical scaling model. In this energy region, b is also represented well by the expression $b = 7.9 + 0.7\ln p$, in agreement with the Regge model.

The question of universality of shrinkage is difficult to answer because of the lack of precise low t, high energy data for the other hadrons. Figure 10b illustrates this point for π^-p, which is the most well-studied reaction next to pp [12]. As we observed earlier, it is not meaningful to look for shrinkage in the region below ~ 100 GeV. With the exception of one experiment, the results of which are systematically high, all experiments agree with one another. The shrinkage is consistent with being the same as in pp, in agreement with universality; but it is also consistent with following the rise of the total cross section, as required by geometrical scaling. More precise data and a longer lever arm (Fermilab Tevatron) are needed to clarify the situation.
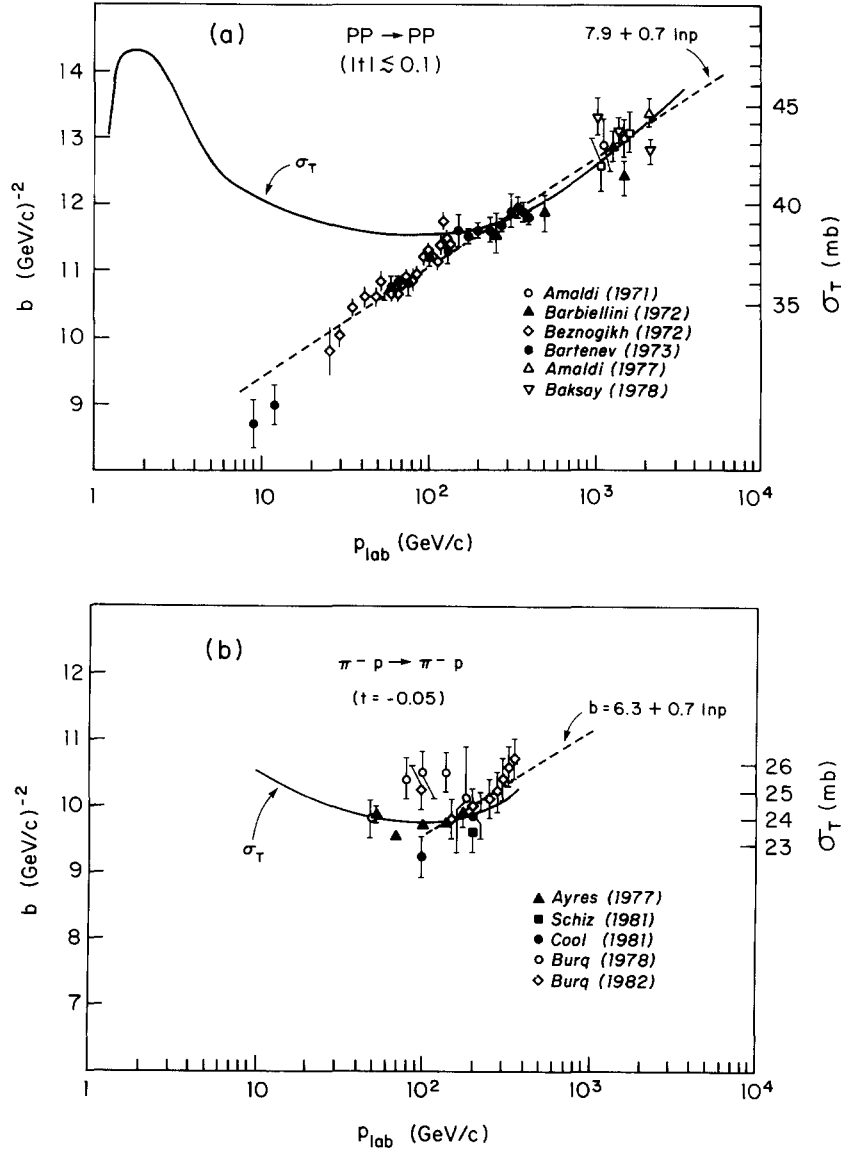
Fig. 10. Slope parameters of forward elastic scattering versus incident hadron momentum (a) for pp and (b) for π^-p. The pion data have been shifted to correspond to $t = -0.05$ (GeV/c)^2, using the t-dependence of b represented by the pion curve in fig. 12. The scales for σ_T relative to those for b were arbitrarily chosen to make σ_T and b coincide at high energies.

A test of universality at $t = -0.2$ (GeV/c)^2, where data exist for all hadrons, is shown in fig. 11. The data were fitted to the form [13]

$$b(p) = b_0 + b_1/p^\beta + b_2 \ln p. \tag{29}$$

The parameters b_0, β and b_2 were kept the same in the particle and antiparticle fits while b_1 was allowed to be different. When β was treated as a free parameter, its value was found to be consistent with 0.5. The term $b_1/\sqrt{p}$ was interpreted as summarizing secondary Regge trajectories and therefore the final
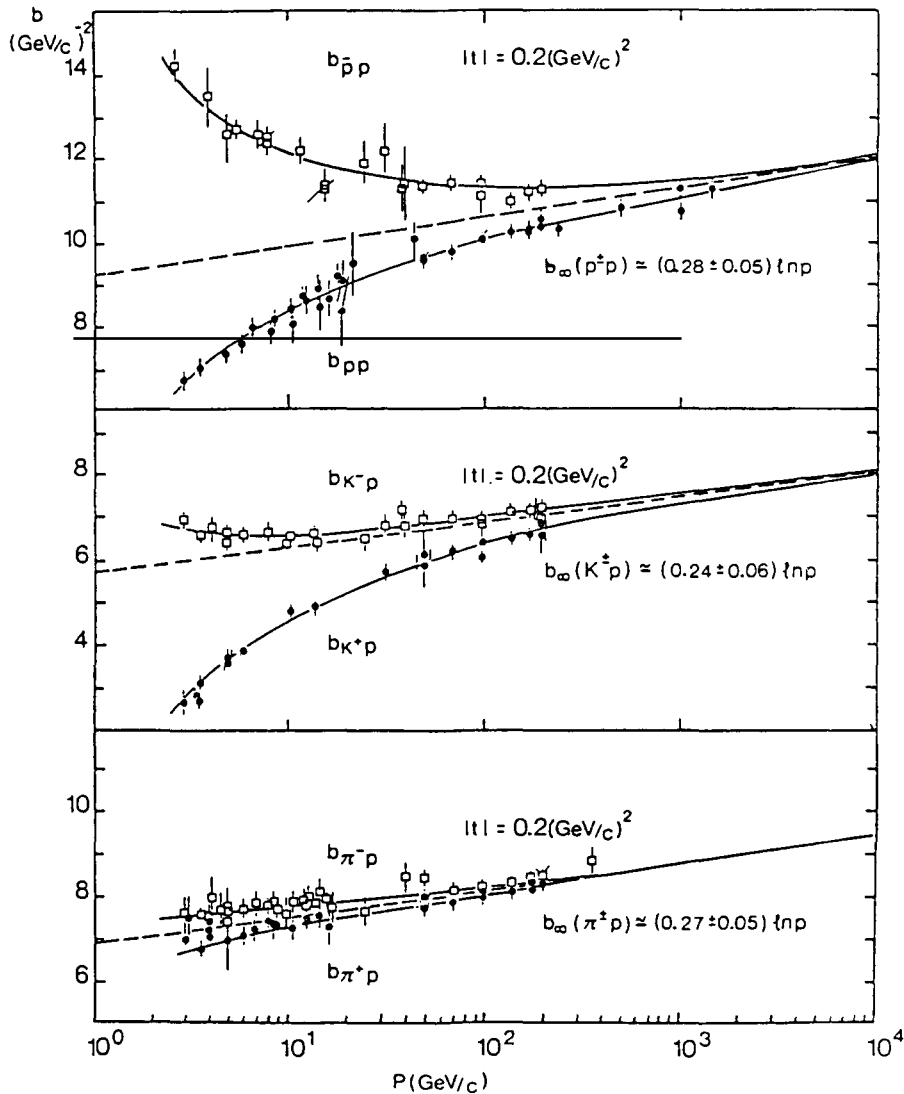
Fig. 11. Elastic slope parameters at $t = -0.2\,(\mathrm{GeV}/c)^2$ versus incident hadron momentum for $p^{\pm}p$, $K^{\pm}p$ and $\pi^{\pm}p$ scattering. The solid curves are fits to the form $b(p) = b_0 + b_1/\sqrt{p} + b_2 \ln p$. The dotted lines represent the expression $b(p) = b_0 + b_2 \ln p$, where b_0 and b_2 are the values determined by these fits [13].

fits were performed with β fixed at 0.5. The values of b_2 obtained by this procedure are approximately the same for all three hadrons and equal to $\sim 0.26 \pm 0.05\,(\mathrm{GeV}/c)^{-2}$. The ratio of any two of the three shrinkage parameters is $\sim 1 \pm 0.3$, consistent with universality. However, as seen in fig. 3, the rise of all total cross sections is also the same within this accuracy and therefore the geometrical scaling model is not ruled out by this result.

The t-dependence of b is shown in fig. 12 for pp and $\pi^{\pm}p$ scattering at 200 GeV [14]. All slopes decrease with increasing t in a very similar way. This continues to be true at low energies, as can be seen by comparing figs. 10 and 11. Many models have been proposed to explain this behavior [15, 16, 17]. A simple phenomenological model [16] that reproduces the t-dependence of b while, at the same
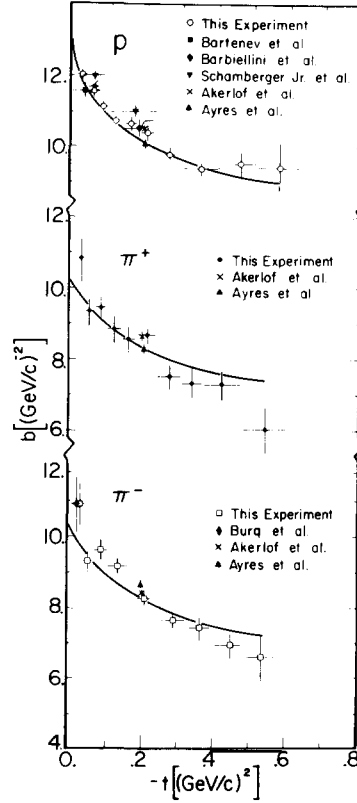
Fig. 12. Elastic slope parameters versus t at 200 GeV/c for pp, π^+p and π^-p scattering (data from ref. [14]). The curves were calculated using eq. (38), as described in the text.

time, predicts the correct s-dependence has interesting theoretical implications and is discussed here in some detail. The model has been constructed for pp scattering but, at high energies, it applies to the other hadrons as well.

The total inelastic cross section at high energies consists of a hard core and a diffractive component (see section 4 and fig. 13a)

$$\sigma_{in}(s) = \sigma_0 + \sigma_D(s) \tag{30}$$

while the ratio of the elastic to the total cross section is constant (see section 2.3)

$$\sigma_{el}/\sigma_T = c. \tag{31}$$

From eqs. (30) and (31), it follows that

$$\sigma_T(s) = \frac{1}{1-c}\left[\sigma_0 + \sigma_D(s)\right] \tag{32}$$

$$\sigma_{el}(s) = \frac{c}{1-c}\left[\sigma_0 + \sigma_D(s)\right]. \tag{33}$$
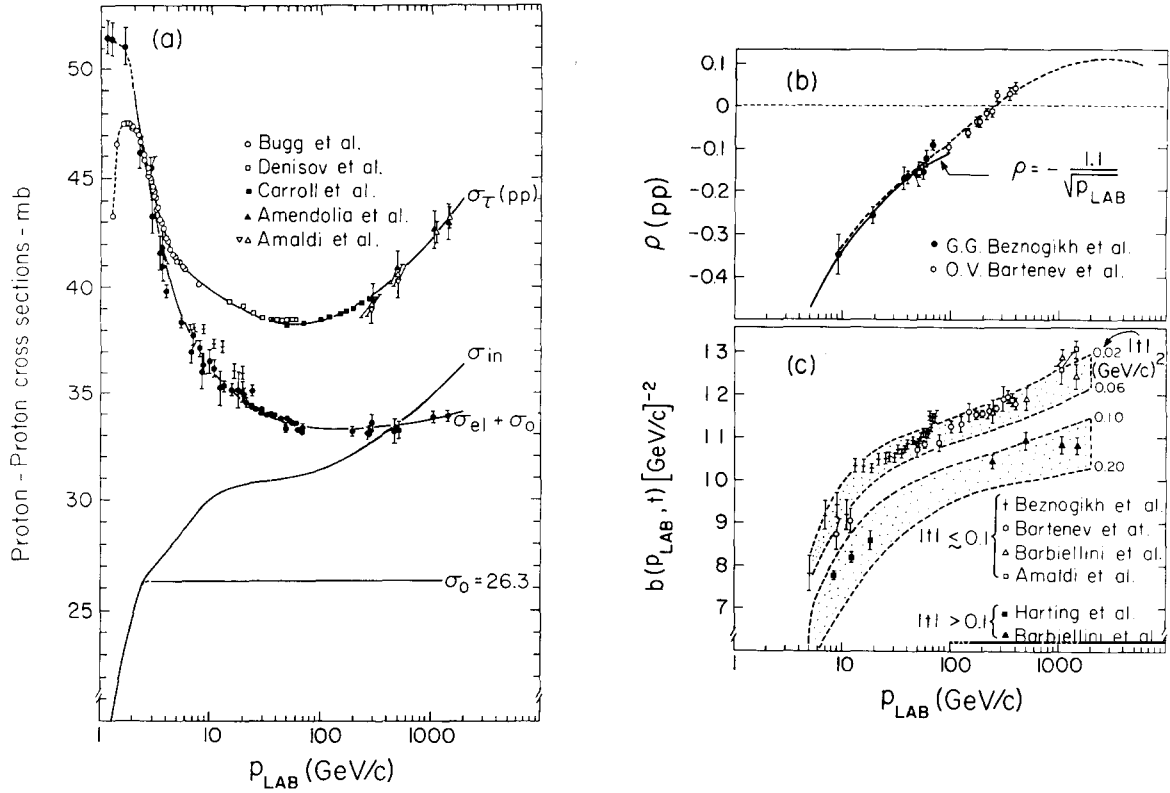
Fig. 13. Proton–proton (a) cross sections, (b) ρ-values, and (c) elastic scattering slope parameters versus laboratory momentum [16]. The curve for σ_T is an empirical fit to the data. The curve for σ_{el} is obtained from σ_T using eq. (41). The inelastic cross section is given by $\sigma_{in} = \sigma_T - \sigma_{el}$. The curves in (c) are calculated using eq. (40).

Eq. (33) suggests that the elastic differential cross section could be written as

$$\frac{d\sigma_{el}}{dt} = \pi \left| A_1 \, e^{b_1 t/2} + A_2(s) \, e^{b_2(s)\, t/2} \right|^2 . \tag{34}$$

The first term in (34) is associated with σ_0 and is assumed to be independent of s, including the slope parameter b_1. In this way, this model differs from other two component models [17]. The second term is associated with $\sigma_D(s)$. Both A_2 and b_2 must be functions of s if the optical theorem and eq. (33) are to be satisfied. The ρ-value is, of course, taken to be zero for both A_1 and A_2. By applying the optical theorem and using (32), we obtain

$$A_1 + A_2(s) = \frac{\sigma_T}{4\pi} = \frac{1}{4\pi(1-c)}\left[\sigma_0 + \sigma_D(s)\right]$$

and therefore

$$A_1 = \frac{\sigma_0}{4\pi(1-c)}, \qquad A_2(s) = r(s)\, A_1$$

where

$$r(s) = \frac{\sigma_D(s)}{\sigma_0} = \frac{\sigma_T - \sigma_{el} - \sigma_0}{\sigma_0} = (1-c)\frac{\sigma_T(s)}{\sigma_0} - 1.$$

(35)

Integrating (34) and using (33) yields

$$\frac{A_1^2}{b_1} + \frac{4A_1A_2}{b_1+b_2} + \frac{A_2^2}{b_2} = \sigma_{el} = \frac{c}{1-c}[\sigma_0 + \sigma_D(s)]$$

which results in

$$b_1 = \frac{\sigma_0}{16\pi c(1-c)}, \qquad b_2 = \beta(s)\,b_1\,; \qquad \beta = \tfrac{1}{2}(3 + r + \sqrt{9 + 10r + r^2}).$$

(36)

Thus, the differential cross section and the overall slope parameter are given by

$$\frac{d\sigma_{el}}{dt} = \frac{1}{(1-c)^2}\frac{\sigma_0^2}{16\pi}e^{b_1 t}[1 + r\,e^{(\beta-1)\,b_1 t/2}]^2$$

(37)

$$b = \frac{d}{dt}\ln\frac{d\sigma}{dt} = b_1\left[1 + \frac{(\beta-1)\,r}{r + e^{-(\beta-1)b_1|t|/2}}\right].$$

(38)

For pp, $\sigma_0 = 26.3$ mb and $c = 0.175$, therefore $b_1 = 9.2\,(\text{GeV}/c)^{-2}$. The value of $r(s)$ is calculated from $\sigma_T(s)$ using eq. (35). At 200 GeV, $r = 0.217$ and $\beta = 3.28$, hence $b(t) = 9.2\,[1 + 0.49/(0.217 + e^{10.5|t|})]$. The solid line in fig. 12 represents this function. The agreement with the data is excellent. For $\pi^- p$ at 200 GeV, $\sigma_T = 24.3$ mb, $\sigma_{el}/\sigma_T = (\sigma_{el}/\sigma_T)_{pp}(\sigma_T^{\pi^- p}/\sigma_T^{pp})^{1/2} = 0.137$ (using eq. (42)), $\sigma_{el} = 0.137\,\sigma_T = 3.3$ mb, $\sigma_D = 3.5$ mb (from refs. [26] and [31], integrating over M_x^2 from 2 GeV^2 to $0.1s$) and $\sigma_0 = \sigma_T - \sigma_{el} - \sigma_D = 17.5$ mb. It is interesting to note that $\sigma_0^{\pi^- p}/\sigma_0^{pp} = 2/3$, consistent with the additive quark model. Using these cross sections, we obtain $r = 0.2$, $\beta = 3.3$, $b_1 = 7.5\,(\text{GeV}/c)^{-2}$ and $b(t) = 7.5\,[1 + 0.45/(0.2 + e^{8.5|t|})]$, which we plot in fig. 12 for $\pi^- p$ and for $\pi^+ p$. Again, the agreement with the data is very good.

At low energies, the total elastic pp scattering is given by (see section 2.3)

$$\sigma_{el} = \frac{c}{1-c}\sigma_{in} + \frac{35}{p}.$$

(39)

The $1/p$ term is presumably coming from an amplitude that is mostly real and therefore

$$\frac{d\sigma_{el}}{dt} = \frac{35}{p}\,b_3\,e^{b_3 t} + \text{eq. (37)}$$

and

$$|\rho| = \frac{((35/p)\,b_3)^{1/2}}{\sigma_T/4\sqrt{\pi}} \cong \frac{1.1}{\sqrt{p}}$$

where $1.1/\sqrt{p}$ is an approximate experimental fit to the p-value (see fig. 13b). For $\sigma_T = 40$ mb, we obtain $b_3 = 2.8$ (GeV/c)$^{-2}$ and hence the entire pp differential cross section is given by

$$\frac{d\sigma_{el}}{dt} = \frac{98}{p} e^{2.8t} + 52 e^{9.2t} (1 + r e^{4.6(\beta-1)t})^2 .$$

(40)

The logarithmic slope parameter, $b = (d/dt) \ln(d\sigma/dt)$, derived from eq. (40) using $\sigma_D = \sigma_{in} - \sigma_0$, is shown against the data at various t-values in fig. 13c. The agreement is remarkably good. Above ~100 GeV, the increase of b with energy given by this form is compatible with the expression $2\alpha' \ln p$, with $2\alpha' = 0.7$ at $t = -0.05$ and $2\alpha' = 0.26$ at $t \cong -0.2$, as required by the data in figs. 10a and 11a.

At the CERN $\bar{p}p$ Collider, the small angle $\bar{p}p$ elastic differential cross section at $\sqrt{s} = 540$ GeV has been measured by experiments UA4 [18] and UA1 [19] in the respective t regions of $0.05 < |t| < 0.29$ and $0.14 < |t| < 0.26$ (GeV/c)^2. By fitting the data to the form $dN/dt = A \exp(bt)$, UA4 obtained $b = 17.2 \pm 1.0$ (± 0.5 systematic uncertainty) (GeV/c)$^{-2}$ while UA1 reported $b = 13.3 \pm 1.5$ (GeV/c)$^{-2}$. In order to compare these values with the above model (eq. (38)), one needs to know the value of r (eq. (35)) and therefore, the value of σ_T. The total cross section as $\sqrt{s} = 540$ GeV was measured by UA4 [18] and was found to be 66 ± 7 mb. Using this value we obtain $b = 16.0 \pm 1.2$ and 11.2 ± 0.2 (GeV/c)$^{-2}$ at $|t| = 0.085$ and 0.178 (GeV/c)^2, respectively, where the values of t represent the mean values of the t-ranges of the two experiments, calculated using the measured slopes. The agreement of the predicted slopes with the experimentally measured ones is satisfactory. The differential cross sections are shown in fig. 14. The solid curve represents eq. (37) with $\sigma_T = 66$ mb, while the broken curves were calculated using $\sigma_T = 66 \pm 7$ mb. The relative and the overall normalization of the two sets of data were adjusted to best fit the curves. With the exception of the edges of the t-range of each data set, where acceptance corrections and systematic effects are large, the curves fit the experimental points well. The disagreement of the experiments in the overlapping t-range indicates the need for more and better data.
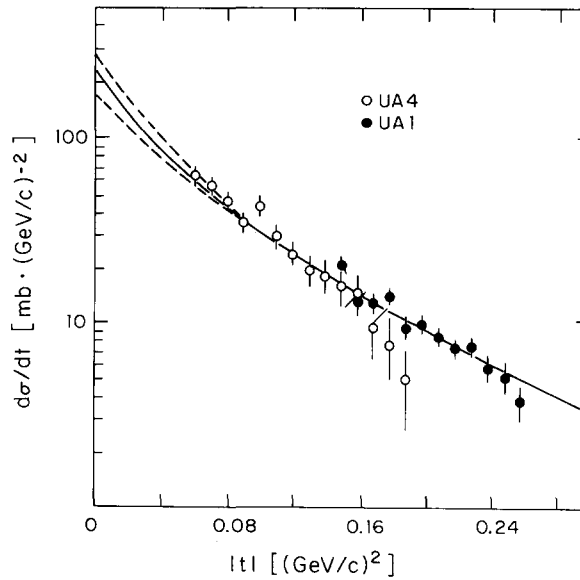

Fig. 14. The differential cross section for $\bar{p}p$ elastic scattering at $\sqrt{s} = 540$ GeV. The data points are from experiments UA4 and UA1 at the CERN $\bar{p}p$ Collider. The curves were calculated using eq. (37) in the text with $\sigma_T = 66 \pm 7$ mb, the value measured by UA4. The normalization of the two data sets is arbitrary.
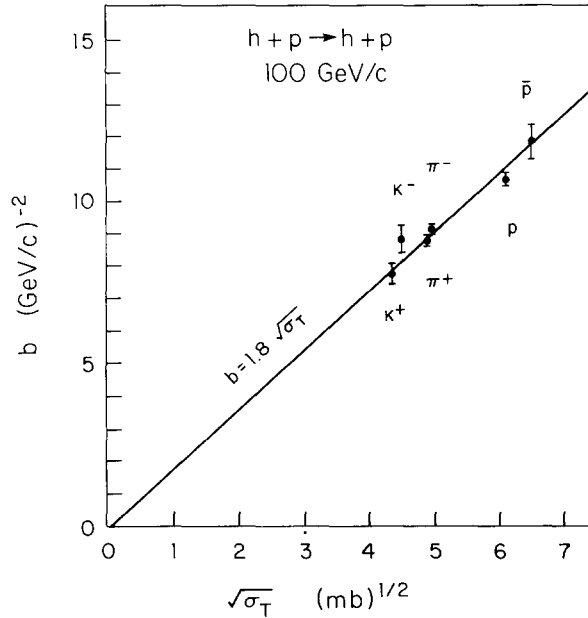
Fig. 15. Hadron–proton elastic scattering slope parameters at $t = -0.05$ $(\mathrm{GeV}/c)^2$ versus $\sigma_{\mathrm{T}}^{1/2}$ at $p_{\mathrm{lab}} = 100\ \mathrm{GeV}/c$ (data from ref. [26]).

A theoretical basis for the model we have presented exists within the Regge framework. As discussed in section 1, the first order pomeron exchange diagrams with $\alpha(t) = 1 + \alpha't$ lead to a total cross section that is constant with energy and to an elastic differential cross section that varies with s as $\exp(2\alpha'\ln s\,t)$, therefore an integrated elastic cross section that decreases with energy as $1/\ln s$. Taking $\alpha' = 0$ results in $d\sigma/dt$ and σ_{el} also being constant with energy. In the absence of contributions from higher order diagrams, the pp cross sections would then be $\sigma_{\mathrm{in}} = \sigma_0$, $\sigma_{\mathrm{T}} = \sigma_0/(1 - c)$ where $c = \sigma_{\mathrm{el}}/\sigma_{\mathrm{T}}$, and $d\sigma/dt = \pi A_1^2\,e^{b_1 t}$ with A_1 and b_1 as given in (35) and (36). The higher order diagrams, which are presumably responsible for the rise of the total cross section, generate an s-dependent term in the inelastic cross section so that $\sigma_{\mathrm{in}}(s) = \sigma_0 + \sigma_{\mathrm{D}}(s)$, as given in eq. (30). Whether the term $\sigma_{\mathrm{D}}(s)$ is entirely or partially diffractive is not relevant to our discussion here. What is relevant is that the same diagrams which generate $\sigma_{\mathrm{D}}(s)$ also generate some elastic cross section. If this happens in such a way that $\sigma_{\mathrm{el}}/\sigma_{\mathrm{T}}$ remains constant, as seems to be the case experimentally, then A_2 and b_2 in eq. (34) are completely determined by the optical theorem. This procedure generates an effective α' which is a function of t and, as we saw earlier, agrees well with the experimental data.

We conclude this section by presenting, in fig. 15, the slope parameter as a function of $\sigma_{\mathrm{T}}^{1/2}$ for various hadrons incident on hydrogen at 100 GeV. To a good approximation, $b \sim \sigma_{\mathrm{T}}^{1/2}$. A theoretical explanation of this relationship is given in section 5.

2.1.2. The real part of the forward nuclear scattering amplitude

The ratio of the real to the imaginary part of the forward nuclear scattering amplitude (ρ-value) for hp $\rightarrow$ hp is shown in fig. 16 as a function of laboratory momentum [21]. Below $\sim 100\ \mathrm{GeV}/c$, ρ is generally large and varies rapidly with momentum; at higher energies, ρ is small and has a smooth energy dependence. This behavior is reminiscent of the variation with energy of the total cross sections (see fig. 3) and of the slope parameter of elastic scattering (see fig. 11). In all three cases, the low energy behavior is presumably due to non-diffractive terms in the cross section that vary rapidly with energy.
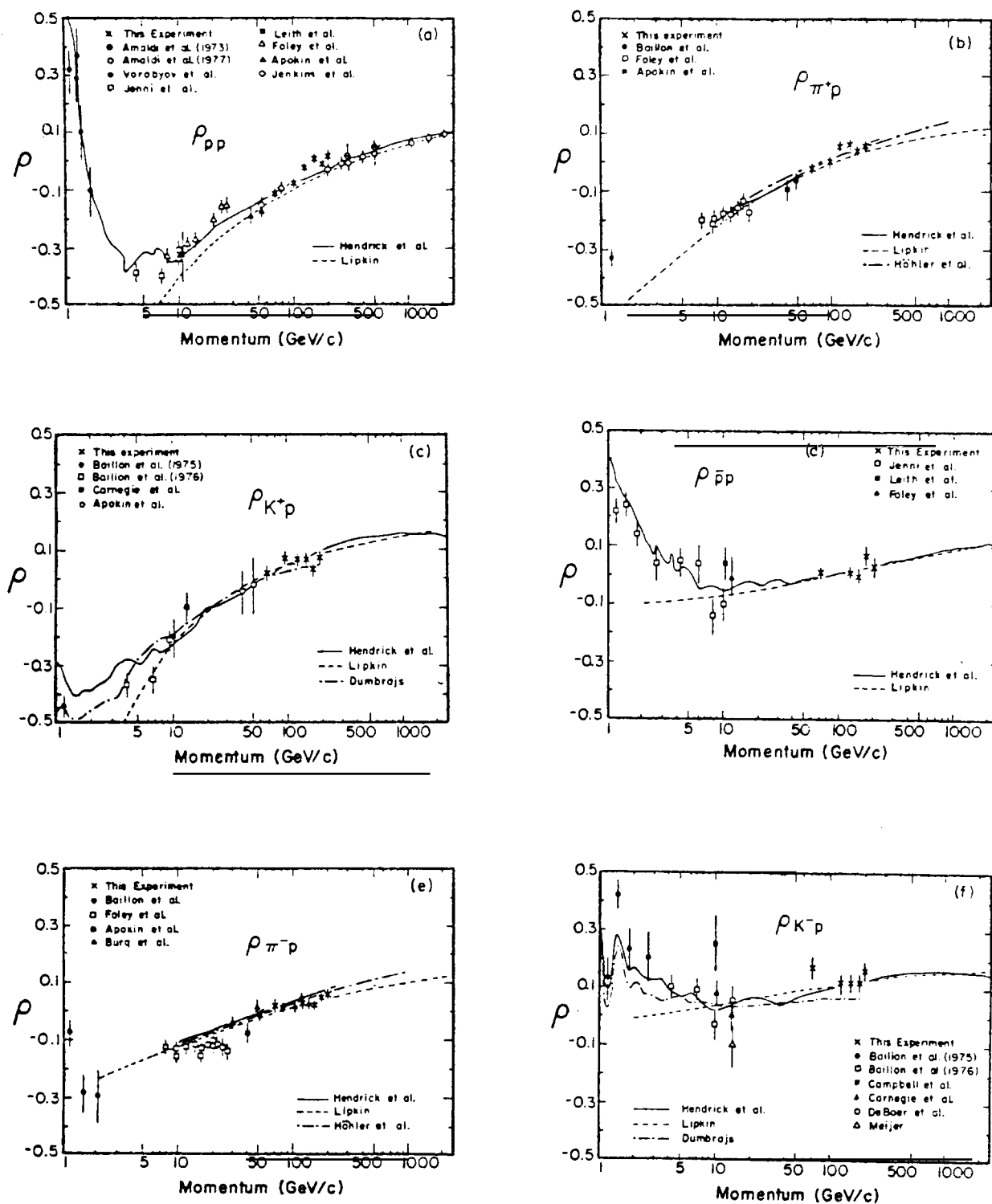
Fig. 16. The ratio of the real to the imaginary part of the forward elastic scattering amplitude as a function of laboratory momentum [21].
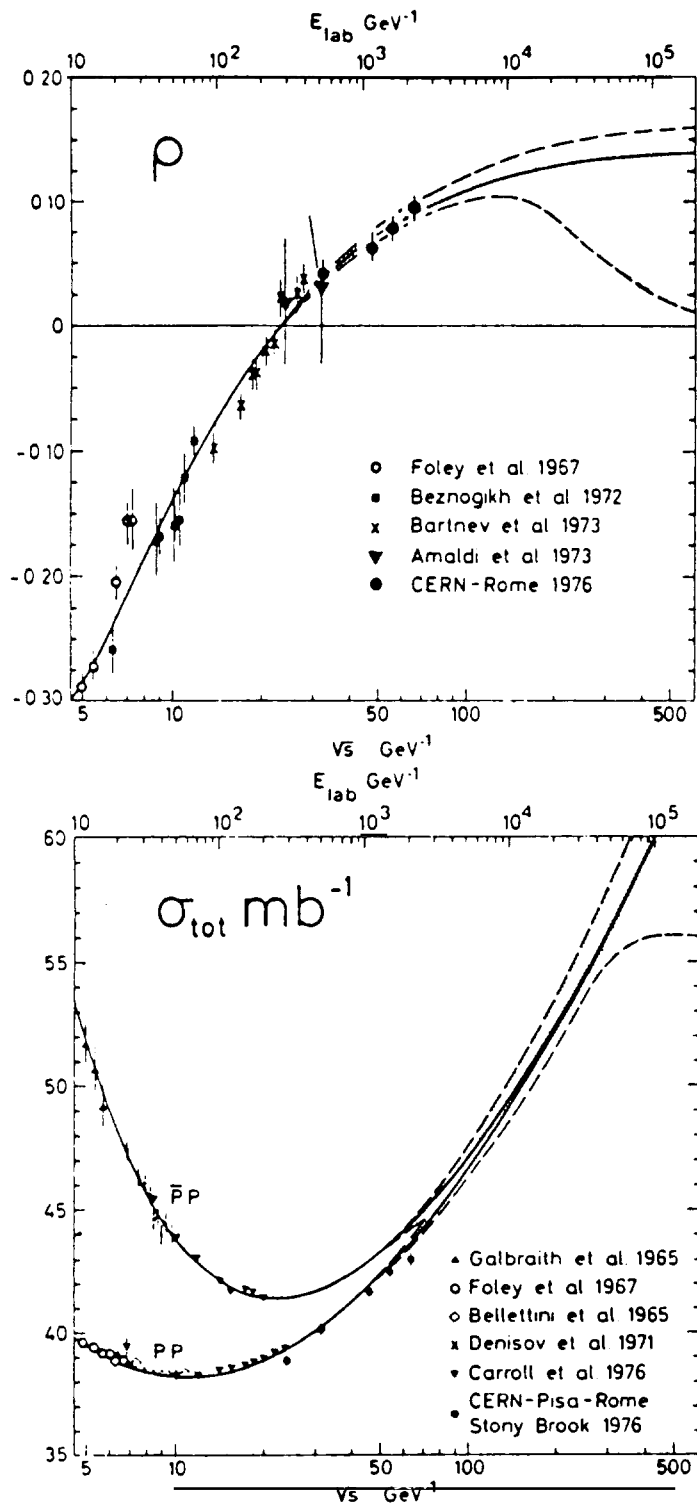
Fig. 17. ρ-values and total cross sections for pp and $\bar{p}$p interactions. The curves are from a dispersion relations fit performed simultaneously on the data for ρ and for σ_T [10].

Dispersion relations reflect the behavior of σ_T upon that of ρ. The relationship of the slope parameter to ρ and σ_T was discussed in the previous section.

The present experimental results on ρ allow predictions to be made on the behavior of total cross sections at energies that are about one order of magnitude higher than the energies at which measurements exist. This is shown [10] for pp in fig. 17. A comparison with critical pomeron Reggeon field theory predictions is presented in section 4 (see fig. 39).

2.2. High t elastic scattering

The most striking feature of the t elastic scattering is the diffraction minimum with the accompanying secondary diffraction maximum (see fig. 1). Naively, the similarity with optics seems quite natural. However, since the high t behavior of hadron scattering is dictated by the dynamics of the strong interaction, the situation is far more complicated here than in optics.

The diffraction minimum is basically due to the interference between two (imaginary) amplitudes of opposite sign and different t-dependence. The critical pomeron theory predicts that the high t behavior of all elastic scattering processes at high energies will be described by the same scaling function. Consequently, the diffraction minimum is expected to occur at the same t-value for all hadrons. Recent results [22] on π^-p scattering at 200 GeV show that, while the structure of the differential cross section is the same as in pp scattering, the t-scale is about a factor of 3 larger. Asymptotically, the t-scales should be the same. According to the arguments presented previously in connection with rising cross sections, slope parameters, and ρ-values, it would appear that 200 GeV should be high enough energy for asymptotic behavior to set in. However, since the position of the minimum can be influenced by small amounts of non-scaling amplitudes, it may be that, in this particular case, asymptopia has not yet been reached. Measurements at the Fermilab Tevatron will, hopefully, clarify the situation.

The detailed features of high t pp scattering are reviewed extensively in ref. [4] along with a discussion of various models proposed for their explanation.

2.3. Total elastic cross sections

The integrated elastic cross sections, hp → hp, are intimately related to the corresponding total cross sections, hp → anything. For example, the pp elastic and total cross sections are shown as a function of laboratory momentum in fig. 13a. The solid curves, drawn through the data for $p_{\text{lab}} > 2\,\text{GeV}/c$, are related by the equation [16]

$$\frac{\sigma_{\text{el}} - B/p_{\text{lab}}}{\sigma_T - B/p_{\text{lab}}} = c \tag{41}$$

where B and c are constants with values $B = 35\,\text{mb} \cdot \text{GeV}/c$ and $c = 0.175$. It follows that $\sigma_{\text{el}} = B/p_{\text{lab}} + c' \sigma_{\text{in}}$, where $c' = c/(1 - c) = 0.212$ and $\sigma_{\text{in}} = \sigma_T - \sigma_{\text{el}}$. This last equation for σ_{el} was used in section 2.1.1 as a starting point in the calculation of the slope parameter. As p_{lab} increases, the ratio $\sigma_{\text{el}}/\sigma_T$ tends to a constant, in agreement with geometrical scaling. Eq. (41) shows the way in which geometrical scaling is approached in pp scattering.

At a given energy, the elastic cross sections of different hadrons incident on protons are related
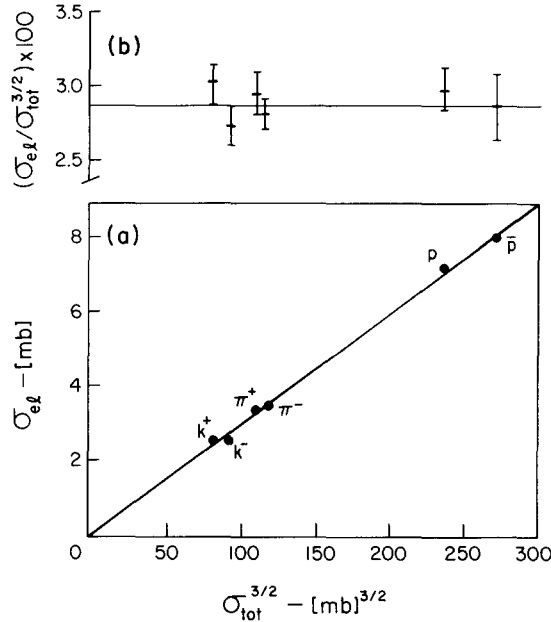
Fig. 18. The ratios $\sigma_{el}/\sigma_T^{3/2}$ and the elastic hadron–proton cross sections for hadron–proton interactions plotted against $\sigma_T^{3/2}$ at $p_{lab} = 100$ GeV/c (ref. [2], data from ref. [26]).

through the equation [2]

$$\sigma_{el}/\sigma_T^{3/2} = c(s) \tag{42}$$

where $c(s)$ is the same for all hadrons. This is shown in fig. 18 for $p_{lab} = 100$ GeV/c. A theoretical explanation of eq. (42) is presented in section 5.

3. Inclusive single diffraction dissociation

The inclusive single diffraction dissociation processes $hp \rightarrow Xp$, $hp \rightarrow hX$ and $pd \rightarrow Xd$, where $h = p^{\pm}$, $\pi^{\pm}$, $K^{\pm}$, have been studied at Fermilab [23–31] and at the ISR [32]. The differential cross sections, $d^2\sigma/dt\, dM_x^2$, are exponential in t, vary as $1/M_x^2$, exhibit small energy dependence and obey factorization rules. The low and high mass diffractive components are related to elastic scattering through the finite mass sum rule. The total single diffraction dissociation cross section increases with energy; while this increase is responsible for only part of the rise of the total inelastic cross section at high energies, the remaining rise can be attributed to inclusive double diffraction dissociation. The charged multiplicity distributions of high mass diffractive states follow a universal Gaussian function that depends only on the available mass for particle production. These and other simple features of diffraction dissociation are discussed in sections 3.1 to 3.6. A general introduction was given in section 1.

3.1. The t, M_x^2 and s-dependence of the diffraction dissociation cross section

In the region $|t| \lesssim 0.1$ (GeV/c)^2, $1 - x \lesssim 0.1$ and for $M_x^2 \gtrsim 5$ GeV^2 the diffraction dissociation cross
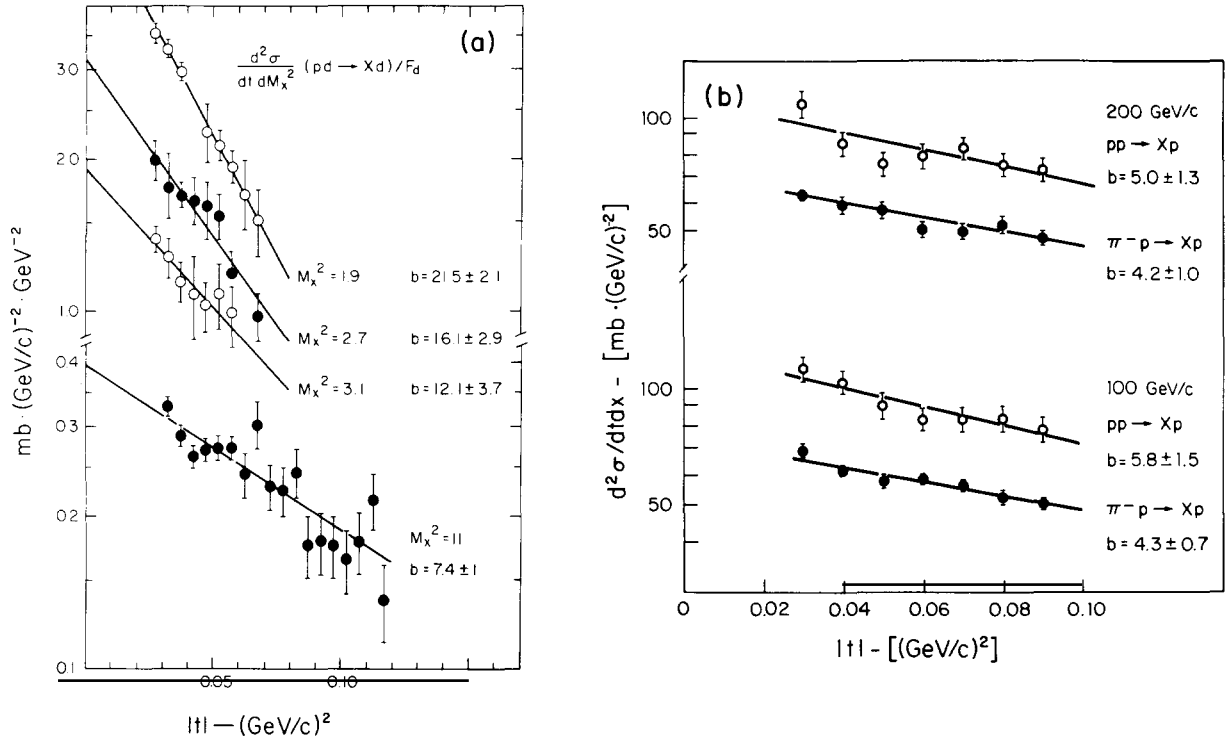
Fig. 19. Differential cross sections versus t (a) for $pp \to Xp$, obtained from $pd \to Xd$ using factorization [25] and (b) for the high mass region of $pp \to Xp$ and $\pi^- p \to Xp$ [31].

section for the inclusive process $h + a \to X + a$ is described well by the expression [27, 28, 31]

$$\frac{d^2\sigma}{dt\,dx} = \frac{A(1 + B/s)}{1 - x} e^{b_D t} + A'(1 - x) e^{b' t} \tag{43}$$

where the constants A, B, b_D, A' and b' depend on the particles h and a. The first term is identified with single diffraction dissociation (see eq. (21)) while the second term is mostly due to non-diffractive contributions. This view is supported by the fact that the first term obeys factorization rules, as discussed in section 3.2, while the second term does not. For $pp \to Xp$, $A'/A \cong 100$, so that at $1 - x = 0.1$ the diffractive and non-diffractive terms are approximately equal while at $1 - x = 0.03$, the diffractive term is about 90% of the inclusive cross section.

The t-dependence is exponential, as expected for diffractive processes (fig. 19). Approximately, $b' = b_D$. Over a wider range of momentum transfer, the slope parameter is found to decrease with t in a way similar to that of elastic scattering [32]. The exponential behavior has been checked [28] for high M_x^2 down to t-values of 0.01 $(GeV/c)^2$. The fact that the cross section appears not to vanish at $t = 0$ is of particular importance to the critical pomeron Reggeon field theory. For $M_x^2 \geq 5\,GeV^2$, the slope parameter is independent of M_x^2 (fig. 20), but for lower masses it increases with decreasing M_x^2 (figs. 19, 20 and 22). This behavior finds an explanation in the finite mass sum rule (see section 3.3).

The high mass diffractive cross section has a $1/(1 - x)$ or $1/M_x^2$ dependence (fig. 21) which, in the Regge picture, arises from triple pomeron dominance (eq. (21)). However, the s-dependence given by
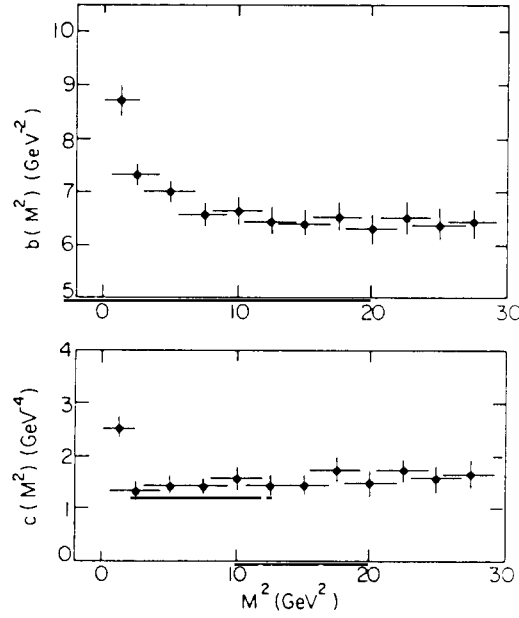
Fig. 20. Diffractive slope and curvature parameters, b and c, from a fit of the form $\exp(bt + ct^2)$ to ISR data for $pp \rightarrow Xp$ [32].
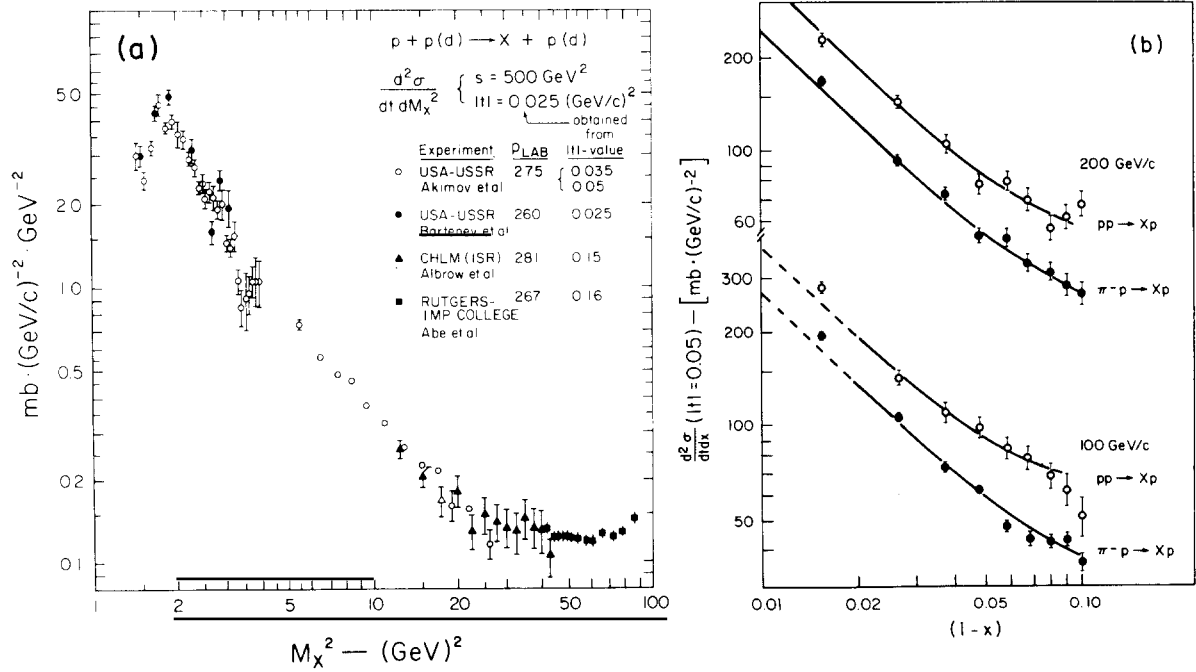

Fig. 21. The diffractive differential cross section plotted against M_x^2 or the Feynman x variable (a) for $pp \rightarrow Xp$ at $t = -0.025\,(\text{GeV}/c)^2$ and $s = 500\,\text{GeV}^2$ [25]; (b) for $pp \rightarrow Xp$ and $\pi^- p \rightarrow Xp$ at $t = -0.05\,(\text{GeV}/c)^2$ and $p_{\text{lab}} = 100$ and $200\,\text{GeV}/c$ [31].
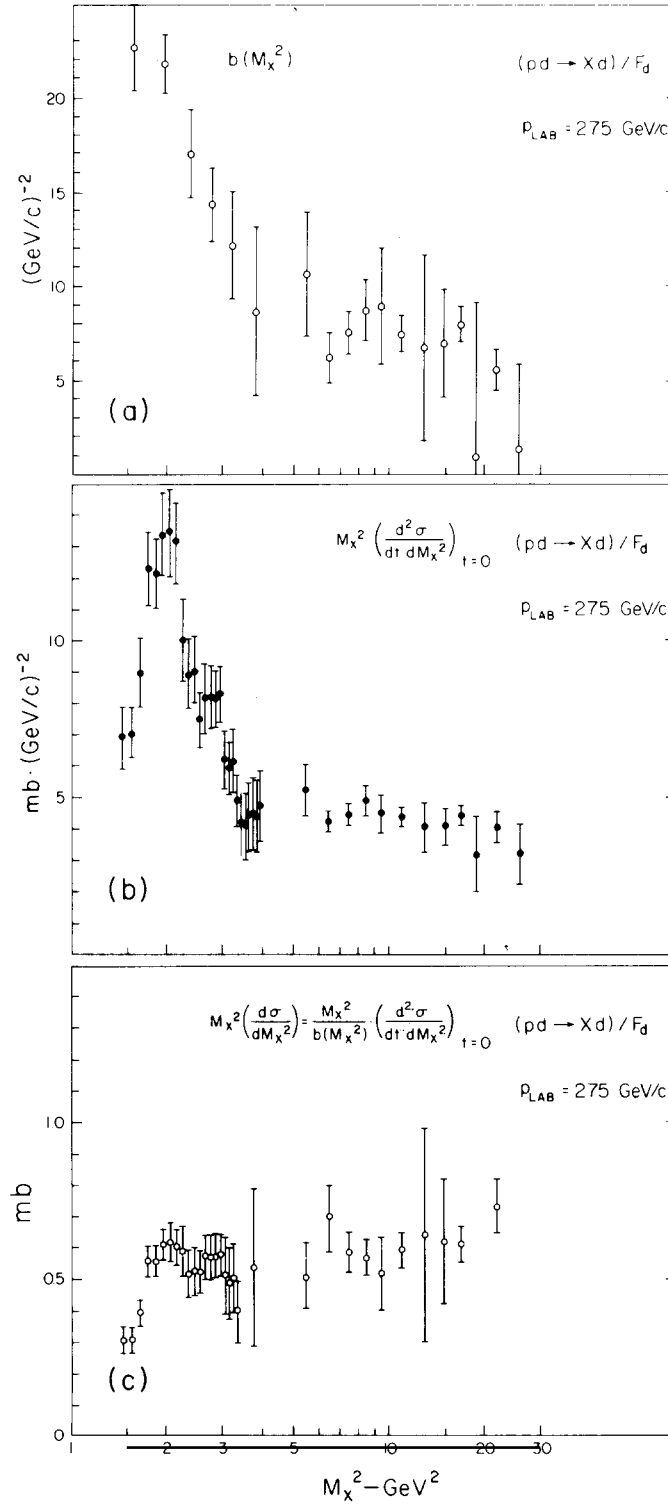
Fig. 22. The slope parameter, (a), and the differential cross section, (b) at the $t = 0$ and (c) integrated over t, plotted against M_x^2 for $pp \rightarrow Xp$ (extracted from $pd \rightarrow Xd$) [25].

the $(1 + B/s)$ factor in (43) is not predicted by the Regge phenomenology. For pp$\rightarrow$Xp, B was measured to be [28] $65 \pm 25 \, \text{GeV}^2$ in the high mass region (error includes systematic uncertainties) and [30] $36 \pm 8 \, \text{GeV}^2$ in the interval $1.2 < M_x^2 < 3 \, \text{GeV}^2$. Within the measurement uncertainties, the two values are the same. In section 5 we will show how this value of B can be estimated from the s-dependence of elastic scattering through the finite mass sum rule.

For $M_x^2 \lesssim 5 \, \text{GeV}^2$, the cross section for fixed t deviates markedly from the $1/M_x^2$ law (fig. 22b). However, the integral over t exhibits approximate $1/M_x^2$ behavior down to $M_x^2 \sim 2 \, \text{GeV}^2$ (fig. 22c). The fast decrease of the cross section below $2 \, \text{GeV}^2$ is presumably due to threshold effects.

As $s \rightarrow \infty$, the diffractice component of the inclusive cross section (first term of eq. (43)) tends to the triple pomeron form given in eq. (21). Taking $\alpha'(t) = 0$, in accordance with our discussion in section 2.1.1, eq. (21) for hp$\rightarrow$Xp may be written as

$$\frac{d^2\sigma/dt\,dx}{\sigma_T} = \frac{[(d\sigma_{el}^{pp}(t)/dt)/16\pi\sigma_T^{pp}]^{1/2}\,g_{PPP}(t)}{1-x}. \tag{44}$$

Using this equation, a recent experiment that studied the diffraction dissociation of $\pi^\pm$, $K^\pm$ and $p^\pm$ on hydrogen [31] extracted for the triple pomeron coupling constant the value of $g_{PPP}(t) = 0.364 \pm 0.025 \, \text{mb}^{1/2}$, independent of t. The ratio $(d^2\sigma/dt\,dx)/\sigma_T$ was found to be the same for all dissociating hadrons, in agreement with the factorization rules discussed below.

3.2. The factorization of the diffractive vertex

As a consequence of factorization, the differential cross sections of a hadron dissociating on different targets scale as the corresponding elastic scattering cross sections while those of different hadrons dissociating on the same target scale as the corresponding total cross sections (see section 1, eqs. (12) and (13)). From the diagrams in figs. 4 and 5, on the basis of which these factorization rules are derived, it is evident that the first rule is quite general while the second is contingent upon the validity of the triple-Regge representation of the diffractive amplitude. Therefore, testing of the second rule provides an indirect way of probing the nature of the diffractive amplitude. The first rule, on the other hand, is expected to hold regardless of the nature of this amplitude. Both rules have been tested experimentally and have been found to hold within experimental accuracy.

The dissociation of the proton on different hadrons, hp$\rightarrow$hX, has been studied for [26, 27] h = $p^\pm$, $\pi^\pm$, $K^\pm$ (Fermilab Single Arm Spectrometer) and for [23, 24, 28] h = d (USA–USSR Collaboration). When the diffractice cross section was expressed in the form given by eq. (43), it was found that the first term, attributed to the triple pomeron amplitude, scales to the corresponding elastic cross section while the second term does not. This result justifies the parametrization used in eq. (43) and the identification of the first term with the diffractive cross section. Figure 23 illustrates a test of this factorization rule for proton dissociation on p and d targets [28]. It is important to notice that the test is performed at the same s-value and therefore at an incident proton laboratory momentum for pd$\rightarrow$Xd which is one half of that for pp$\rightarrow$Xp.

The dissociation of different hadrons on protons, hp$\rightarrow$Xp, has been studied at Fermilab for h = $p^\pm$, $\pi^\pm$, $K^\pm$ at 100 and 200 GeV/c by a Rockefeller University group [31]. The 100 GeV/c results on factorization are presented in fig. 24. At each beam momentum, factorization was found to hold within the experimental uncertainty of $\leq 10\%$.
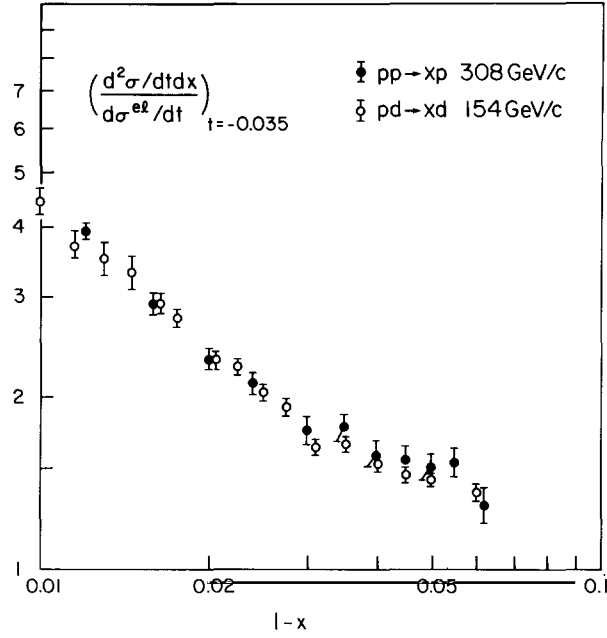
Fig. 23. Factorization test: The ratio of the diffractive to the elastic differential cross sections at fixted t versus the Feynman variable $1-x$ for pp→Xp at 308 GeV/c and pd→Xd at 154 GeV/c (same s-value) [28].
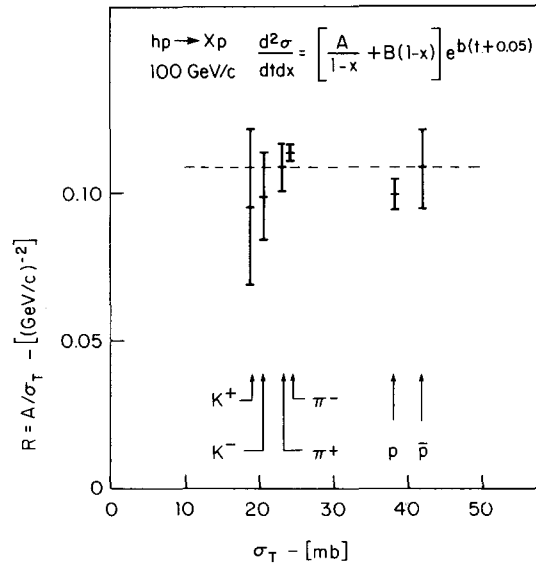

Fig. 24. Factorization test: The ratio of the diffractive to the total cross sections at 100 GeV/c for $p^{\pm}$, $\pi^{\pm}$ and $K^{\pm}$ dissociating on protons [31].

3.3. The finite mass sum rule and the low mass enhancement of diffraction dissociation

The inclusive diffractive cross section consists of elastic scattering, of the low mass "resonance region" or enhancement, and of the high mass continuum. This is illustrated in fig. 25 which shows the differential cross section for $pd \to Xd$ as a function of M_x^2 at fixed t. As discussed in section 1, the three mass regions are related through the finite mass sum rule (eq. (14)). An accurate test of this rule was performed [25] on $pd \to Xd$. Figure 26 shows this test for $|t| = 0.035$ $(GeV/c)^2$. According to eq. (14), one should plot the quantity $\nu(d^2\sigma/d\nu\, dt)$ versus ν, where $\nu = M_x^2 - M_h^2 - t$. However, at fixed t, $d\nu = dM_x^2$ and therefore one can plot $\nu(d^2\sigma/dt\, dM_x^2)$ versus M_x^2, as was done in fig. 26. For purposes of easier visualization, the term $|t|(d\sigma_{el}/dt)$ is represented in this figure as half a Gaussian function. The extrapolation of the high mass $\nu(d^2\sigma/d\nu\, dt)$ into the low mass region represents well the average behavior of the data in this region, as required by eq. (14). The FMSR was tested at various t-values in the range $|t| \lesssim 0.1$ $(GeV/c)^2$ and was found to hold within the experimental accuracy of a few percent.

The behavior of the low mass enhancement with t (fig. 22) can now be understood [33] in terms of the FMSR. As $t \to 0$, the term $|t|$ $(d\sigma_{el}/dt) \to 0$ and therefore, in order for the rule to continue to hold at
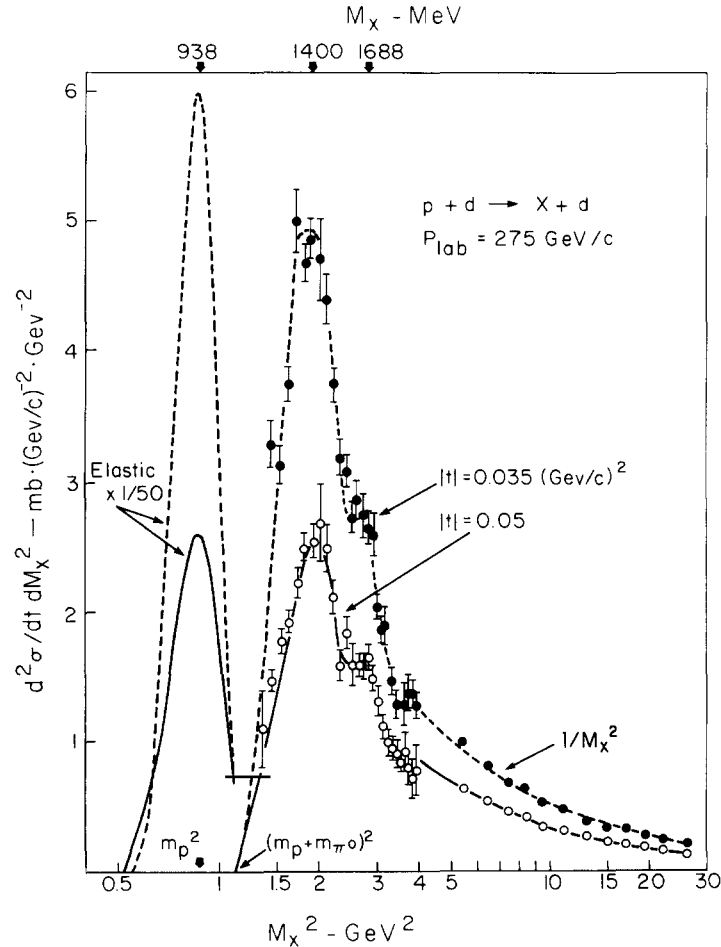

Fig. 25. Differential cross section at fixed t versus M_x^2 for $pd \to Xd$ at 275 GeV/c [25].

$$\nu \left.\frac{d^2\sigma}{dt\,dM_X^2}\right|_{|t|=0.035} \quad (p+d \rightarrow X+d)/F_d$$
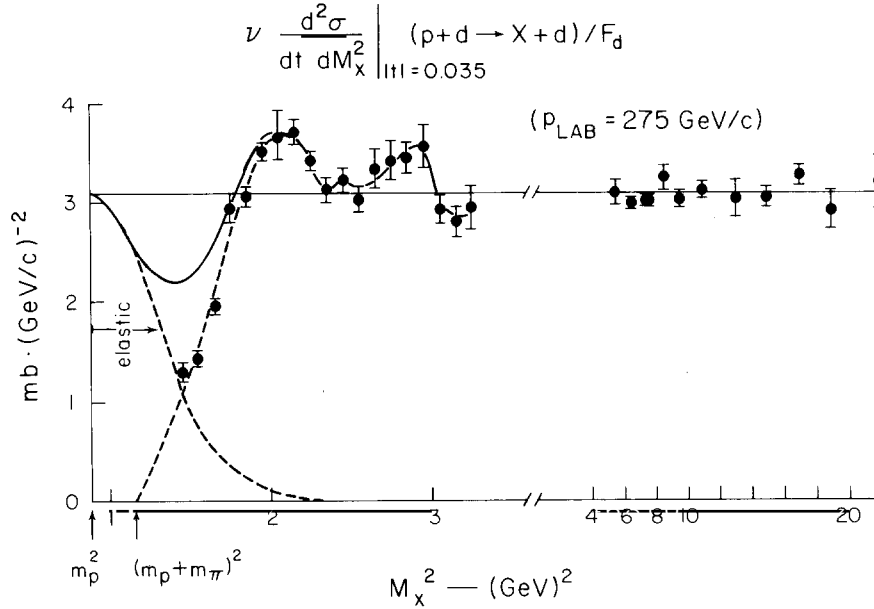

Fig. 26. Test of the first moment finite mass sum rule: The fit to the high mass data for $\nu\,d^2\sigma/dt\,d\nu$ at fixed t, where $\nu = M_X^2 - M_p^2 - t$, extrapolated into the low mass region averages over the values of $\nu\,d^2\sigma/dt\,d\nu$ in this region, including the value of $|t|\,d\sigma/dt$ for elastic scattering which, for pictorial reasons, is represented in this figure as half a Gaussian function [25].

small t-values, the low M_X^2 region must have a large b-slope. Indeed, in the low mass region, the b-slope increases with decreasing M_X^2 in such a manner as to satisfy the FMSR. This behavior has also been observed to occur in pion and kaon dissociation [34]. In all cases, the slope of the low mass enhancement is about twice as large as the slope of elastic scattering. These enhancements are the N*(1400) in pp→Xp, the A₁(1100) in πp→Xp and the Q(1300) in Kp→Xp. The value of $M_X^2 - M_h^2 \cong \nu$ at the enhancement is approximately the same in all three cases. In no case is the entire enhancement consistent with being a resonance. As mentioned earlier, the integral over t of the low mass diffractive cross section follows the $1/M_X^2$ law (see fig. 22c) and has the same s-dependence as the high mass cross section. This suggests that the amplitude responsible for the low mass enhancement is of the same nature as the amplitude for high mass diffraction and therefore it should follow the factorization rules discussed in the previous section. The consequences of this observation are discussed in section 5.

3.4. Total diffraction dissociation cross section

The total cross section for single diffraction dissociation is obtained by integrating the differential cross section (see eqs. (43) and (44)). After integrating over t, the low mass enhancement behaves as $1/M_X^2$ (see fig. 22c). Thus, the lower limit of integration over M_X^2 is $\sim 1.5\,\text{GeV}^2$, while the upper limit, given by the coherence condition, eq. (7), is $M_X^2 = M_p^2 + 0.15s$. Hence, $\sigma_{\text{SD}} \cong (A/b_D)\,(1 + B/s)\ln(0.6 + 0.1s)$. For pp→Xp, the value of $(A/b_D)\,(1 + B/s)$ at 200 GeV/c, obtained from eq. (44) using eq. (40), is 0.75 ± 0.05 mb. Taking $B = 36 \pm 8\,\text{GeV}^2$, which is the experimental value at low masses given in section 3.1 (see also section 5), we obtain

$$\sigma_{\text{SD}}(\text{pp} \rightarrow \text{Xp}) = (0.68 \pm 0.05)\left(1 + \frac{36 \pm 8}{s}\right)\ln(0.6 + 0.1s). \tag{45}$$

At $p_{lab} = 200\,\text{GeV}/c$, $2\sigma_{SD}^{pp} = 5.5\,\text{mb}$. The cross sections for the dissociation of other hadrons may be obtained from (45) using the factorization rules discussed in sections 1 and 3.2.

3.5. Charged multiplicities of high mass diffractive states

The charged multiplicity distribution of high mass diffractive states of hadrons is described well by the Gaussian function [35]

$$P_n = \frac{2}{\sqrt{2\pi}\,D}\, e^{-(n-n_0)^2/2D^2} \tag{46a}$$

$$n_0 = 2M^{1/2} \; (M \text{ in GeV}) \text{ [see also eq. (48)]} \tag{46b}$$

$$n_0/D = 2 \tag{46c}$$

where P_n is the (normalized) probability that the diffractive state decays into n charged particles and M is the mass available for pionization (figs. 27 and 28). Experimentally, one observes positive values of n only. This shifts the average multiplicity by $\sim$4% above the value of n_0 and the width down by $\sim$6% so that $\langle n \rangle = 2.08M^{1/2}$ and $\langle n \rangle/D = 2.2$, as shown in fig. 27.

The distribution represented by eq. (46) satisfied KNO scaling [36]; i.e., the product $P_n \cdot n_0$ is a function of n/n_0 only and not a function of M:
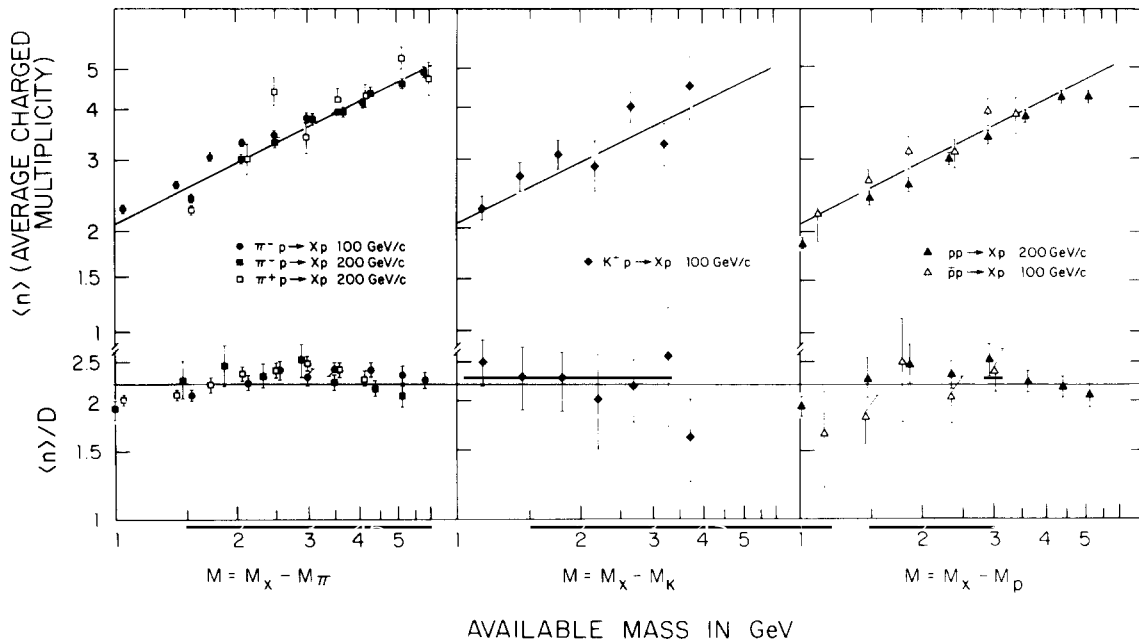

Fig. 27. Average charged multiplicities and ratios of the average $\langle n \rangle$ over the width D, where $D = (\langle n^2 \rangle - \langle n \rangle^2)^{1/2}$, as a function of available mass for high mass diffractive states of hadrons. The curves represent $\langle n \rangle = 2.08\,M^{1/2}$ and $\langle n \rangle/D = 2.2$, as discussed in the text [35].
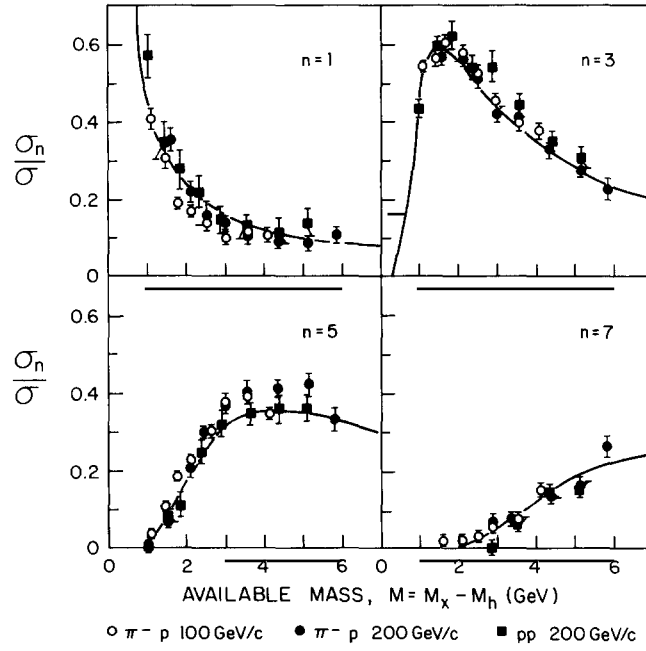
Fig. 28. Charged multiplicity fractions versus available mass for the diffractive state X produced in pp → Xp and $\pi^- p \to Xp$ [35].
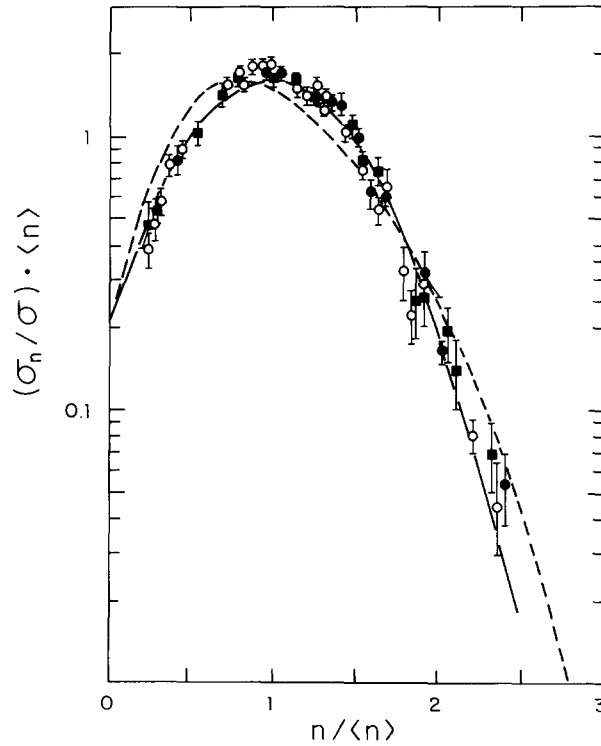

Fig. 29. The product $(\sigma_n/\sigma) \cdot \langle n \rangle$ versus $n/\langle n \rangle$ for the data presented in fig. 28. The solid line represents the Gaussian function discussed in the text (eq. (47)). The broken line is from a fit to the inclusive data hp → anything [35].

$$P_n \cdot n_0 = \sqrt{\frac{8}{\pi}}\, e^{-2(1-n/n_0)^2} \,. \tag{47}$$

Figure 29 shows $P_n \cdot \langle n \rangle$ versus $n/\langle n \rangle$ for diffractive masses produced in $\pi^- p \to Xp$ and $pp \to Xp$. Neglecting the small difference between $\langle n \rangle$ and n_0, formula (47) fits the diffractive data well but does not agree with the data of the fully inclusive reactions $\pi p \to$ anything and $pp \to$ anything which are represented by the dotted curve in fig. 29. However, an analysis of the inclusive data in terms of diffractive and non-diffractive components shows that each component is described well by eq. (46) provided the appropriate available mass is used in each case [37]. Figures 30 and 31 illustrate the application of eq. (46) to the pp and $\bar{p}p$ systems. The available mass was taken to be $M = \sqrt{s} - 2M_p$ for the "hard core" cross section ($\sigma_0 = 26.3$ mb), $M = \sqrt{s}$ for the $\bar{p}p$ annihilation cross section and $M = M_x - M_p$ for the diffractive masses. The agreement with the data is excellent.

Recently, the charged multiplicity distribution for $\bar{p}p \to$ anything at $\sqrt{s} = 540$ GeV was measured at the CERN $\bar{p}p$ Collider [39, 40]. With single diffraction dissociation excluded in the trigger, it was found that [39] $\langle n \rangle = 28.9 \pm 0.4$ and $\langle n \rangle/D = 1.88 \pm 0.05$. The shape of the KNO distribution was reported [39,
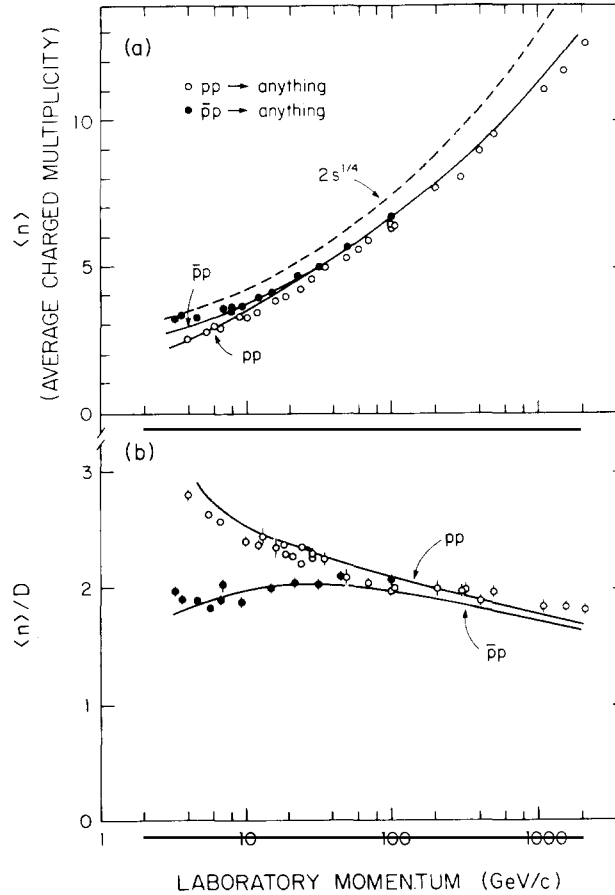

Fig. 30. The average charged multiplicity and the ratio of the average to the width as a function of p_{lab} for $pp \to$ anything and $\bar{p}p \to$ anything. The solid curves were calculated using eq. (46) at the appropriate available mass of the diffractive and non-diffractive components of the inelastic cross section.
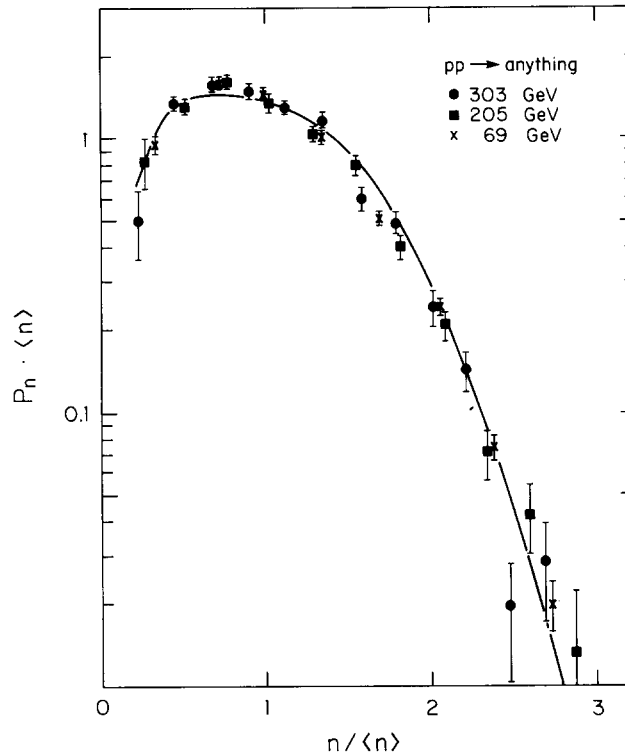
Fig. 31. KNO-scaling distribution for charged particles in pp→anything. The curve was calculated using eq. (46) separately for the diffractive and non-diffractive components of the inelastic cross section.

40] to be non-Gaussian and similar to the shape of the pp inclusive distribution shown in fig. 31. According to eq. (46), the non-diffractive "hard core" collisions should yield $\langle n \rangle = 2s^{1/4} = 46.5$ and a Gaussian KNO distribution with $\langle n \rangle / D = 2$. The obvious disagreement of this prediction with the data can be reconciled by taking into account the effect of double diffraction dissociation and by modifying the M-dependence of the average charged multiplicity in eq. (46b) in such a way as to preserve the prediction $n_0 = 2\sqrt{M} = 2s^{1/4}$ up to $\sqrt{s} \sim 60$ GeV but extrapolate to the measured value at $\sqrt{s} = 540$ GeV. The shape of the multiplicity distribution given by eqs. (46a) and (46c) is not affected by this modification and the idea of universality, as described in ref. [39], remains unchanged.

The double diffraction dissociation cross section at $\sqrt{s} = 540$ GeV is estimated to be about 7 mb (see section 4). At the ISR ($\sqrt{s} \sim 60$ GeV), the single diffraction dissociation cross section, calculated using eq. (45) and multiplying the result by 2 to account for either proton dissociating, is 8 mb, while double diffraction is estimated to be about 2 to 3 mb. Thus, even though single diffraction is not included in the SPS Collider data, the fraction of diffractive to hard core events is approximately the same as at the ISR. At the same time, with a $1/M_x^2$ dependence of diffractive cross sections and a cut-off at $M_x^2 \cong 0.1s$, the average multiplicity for single diffraction at the ISR or double diffraction at the SPS Collider is approximately one-half of the corresponding multiplicity of the hard core. From these considerations it follows that the multiplicity distribution of the SPS Collider events with single diffraction excluded should look approximately the same as that of ISR inclusive events, as is the case experimentally. Clearly, in order to compare "hard core" multiplicities, one has to exclude all diffractive events, single

and double diffractive alike. A proposal to measure multiplicities separately for hard core, single and double diffraction dissociation at $\sqrt{s} = 2000$ GeV has been presented at Fermilab [41].

As mentioned above, in order to predict correctly the average charged multiplicity at $\sqrt{s} = 540$ GeV, formula (46b) must be modified. The formula

$$n_0 = 2 + 0.13 \ln M^2 + 0.18 (\ln M^2)^2 \tag{48}$$

reproduces the data well up to $\sqrt{s} \sim 60$ GeV and yields the experimentally measured value at $\sqrt{s} = 540$ GeV, provided double diffraction dissociation is taken into account. For the hard core, one should use s in place of M^2. For the 26.3 mb of hard core cross section, eq. (48) evaluated at $\sqrt{s} = 540$ GeV gives $n_0 = 32.1$. With an admixture of 7 mb of double diffraction dissociation, having about one-half the hard core multiplicity, the value of 32.1 is reduced to 28.8 as required by the data. A different admixture of diffractive events would require a different formula for n_0 to bring agreement with the data. The need for measuring separately the multiplicities of the different components of the cross section cannot be overemphasized.

3.6. Diffractive pseudo-rapidity distribution

The angular or pseudo-rapidity distribution of charged particles from high mass diffractive states provides a useful tool for studying the mechanism of diffractive production and/or decay. There are basically two groups of models for diffraction dissociation, resulting in two distinct pseudo-rapidity distribution shapes: Fireball-type models [42] which assume isotropy in the center of mass of the diffractive state, and multiperipheral-type models [43]. For an isotropic decay of a diffractive state moving along the beam direction, the charged-particle pseudo-rapidity distribution in the beam-beam center of mass system is given by

$$\frac{dn_c}{d\eta} = \frac{2n_c}{(e^{\eta_x} + e^{-\eta_x})^2}; \qquad \eta_x = \eta - \bar{\eta} \tag{49}$$

where η_x is the pseudo-rapidity of a particle of polar angle θ_x in the center of mass of the state,

$$\eta_x = -\ln \tan(\theta_x/2). \tag{50}$$

n_c is the number of charged particles in the decay and $\bar{\eta}$ is their average pseudo-rapidity,

$$\bar{\eta} = \ln(s^{1/2}/M_x). \tag{51}$$

This distribution, plotted in fig. 32, is very similar to a Gaussian function with a standard deviation

$$\sigma_\eta(\text{fireball}) \cong 0.7. \tag{52}$$

Thus, fireball models predict diffractive clusters of constant rapidity width independent of the mass of the dissociating state. On the other hand, multiperipheral models predict clusters that stretch from the maximum available value of rapidity, $|y_m| = \ln(s^{1/2}/m_p)$, to an inner edge given by $\eta_e = \ln(m_p s^{1/2}/M_x^2)$. The width of these clusters,
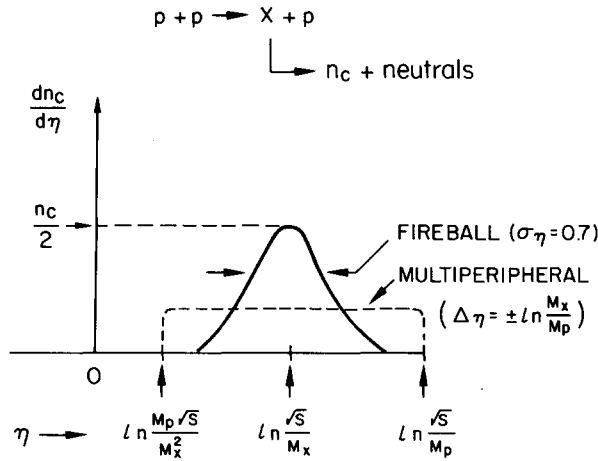
$P_{ISR} = 31.4$ GeV/c , n = 8

Fig. 32. Pseudo-rapidity distribution of charged particles from the decay of a diffractive state X of mass M_x for pp→Xp at (c.m. energy)^2 = s.
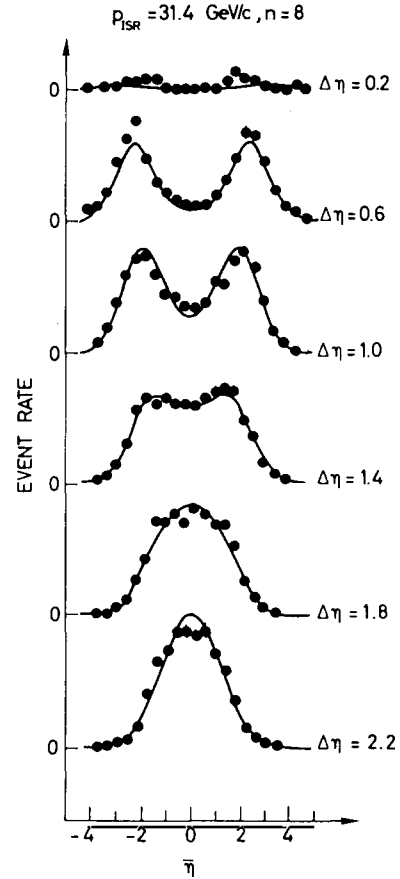
Fig. 33. Distributions of the mean pseudo-rapidity $\bar{\eta}$ for events with a given $\Delta\eta$ and fixed charged multiplicity from pp collisions at P_{ISR} = 31.4 GeV/c at the ISR [45].

$$\Delta\eta \text{(multiperipheral)} = \pm\ln(M_x/m_p) \tag{53}$$

increases with M_x and for $M_x = 4$ GeV it is already twice as large as the fireball width. Therefore, it appears that it should be quite possible to discriminate between the two types of models by simply measuring the width of high mass diffractive clusters as a function of the mass [44].

Diffractive pseudo-rapidity distributions were studied in two experiments at the ISR: The Pisa–Stony Brook experiment [45] and the CHLM collaboration [46]. Results from the Pisa–Stony Brook experiment (see figs. 33 and 34) show that the pseudo-rapidity distribution for diffractive events of a given charged multiplicity (corresponding to a given M_x) is consistent with a Gaussian function of width ±0.6 to ±1.0 and therefore consistent with eqs. (49) and (52). This experiment did not measure the diffractive mass by the recoil technique, but the mass can be obtained from the average pseudo-rapidity of the secondaries using eq. (51). The average pseudo-rapidity of the diffractive peaks in fig. 33 is $\bar{\eta} \cong 2$; this corresponds to a mass of $M_x = s^{1/2} e^{-\bar{\eta}} = 8.5$ GeV for which the multiperipheral model would predict a width of $\Delta\bar{\eta} = \pm 2.1$. The measured width of ±0.6 to ±1.0 favors the fireball model [47].

PISA STONY BROOK

CLUSTERING OF EVENTS IN THE $\bar{\eta}$, $\Delta\eta$ PLANE
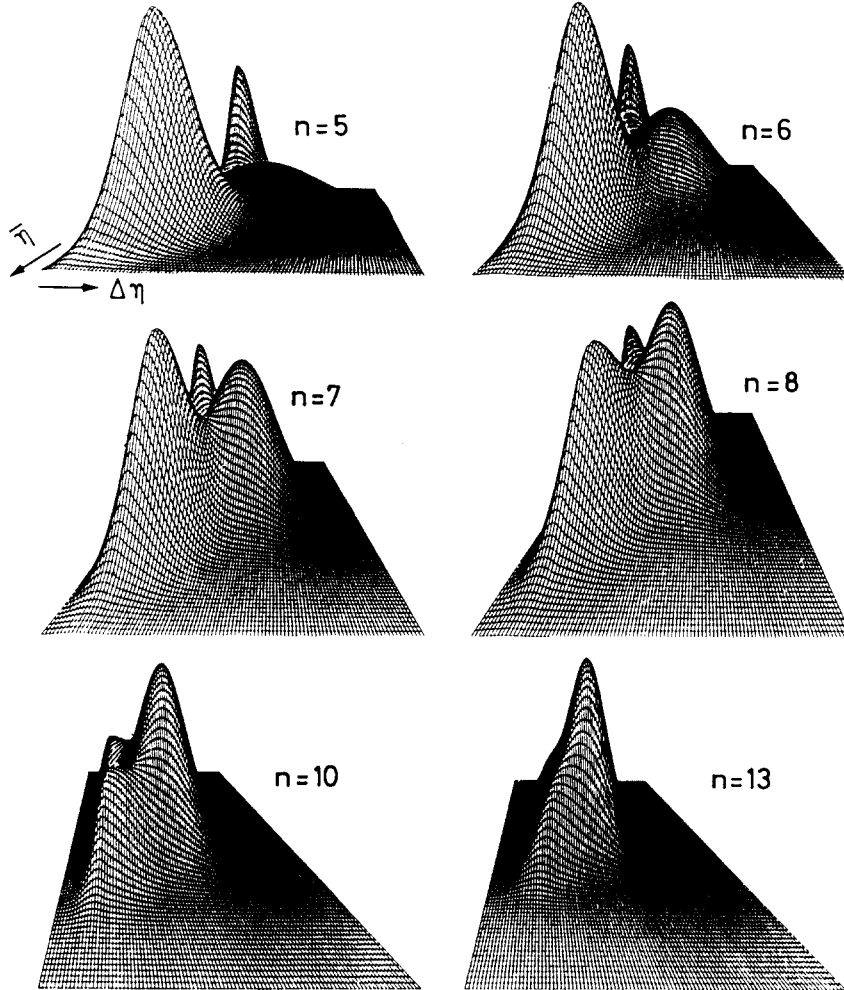
P_{ISR} = 31.4 GeV/c

Fig. 34. The mean pseudo-rapidity $\bar{\eta}$ versus the width $\Delta\eta$ at various charged multiplicities for events from pp collisions at $P_{ISR} = 31.4\,\mathrm{GeV}/c$ at the ISR [45].

The CHLM data seem to contradict this conclusion. These data are presented in figs. 35, 36 and 37. Figure 35 shows typical differential cross sections and associated charged-particle rapidity distributions. As seen in the lower part of fig. 35a, the "diffractive" clusters are centered properly at $y_c = -\ln(s^{1/2}/M_x)$ and their outer edges extend all the way to the kinematic limit of the rapidity range as expected by the multiperipheral model. According to this model, the inner edges of these clusters should be separated by a pseudo-rapidity interval of $\ln(M_x/m_p)^2$. Figure 36 shows the inner edges of clusters for different values of M_x^2 after shifting them by $\ln(M_x/m_p)^2$ and normalizing them to the single particle inclusive distribution. The data for all M_x^2 values now coincide, indicating that the inner edges are indeed
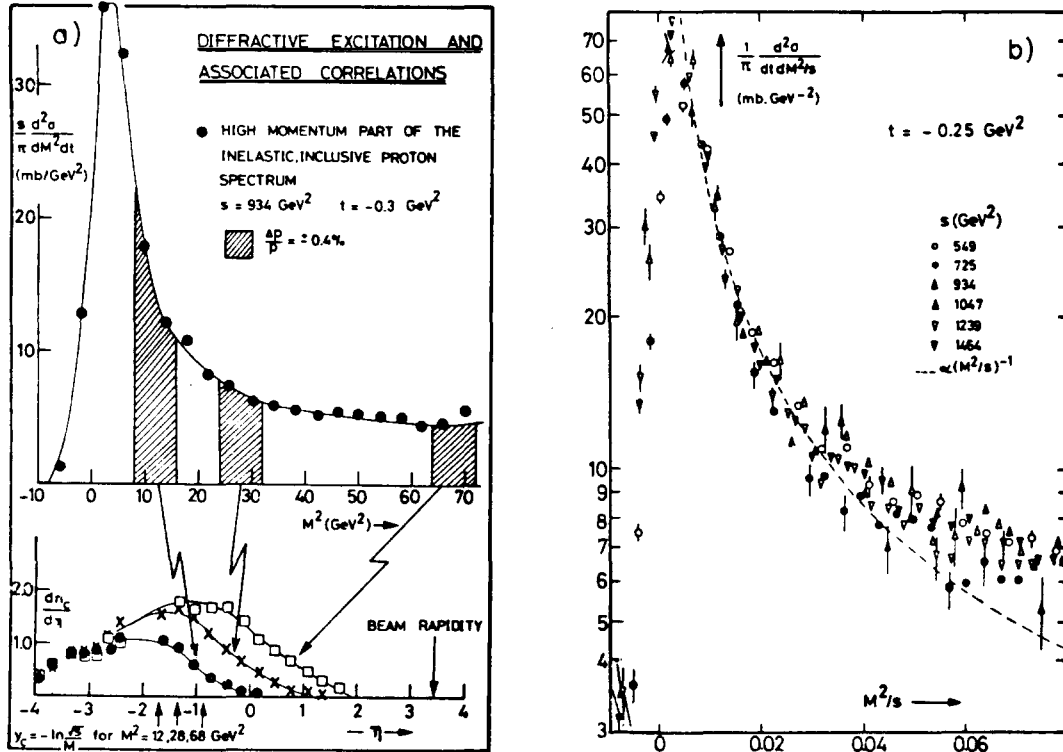
Fig. 35. Typical inclusive differential cross sections for pp → pX and associated charged-particle pseudo-rapidity distributions. (a) The upper part shows the cross section as a function of M_x^2 for $t = -0.3\ \text{GeV}^2$ and $s = 934\ \text{GeV}^2$. The lower part shows the pseudo-rapidity distribution observed in coincidence with leading protons corresponding to $M^2 = 12 \pm 4$, 28 ± 4 and $68 \pm 4\ \text{GeV}^2$ (from ref. [46]). (b) The invariant differential cross section as a function of M^2/s for various values of s. The dashed line shows a dependence of the form $(M^2/s)^{-1}$ (from ref. [32]).
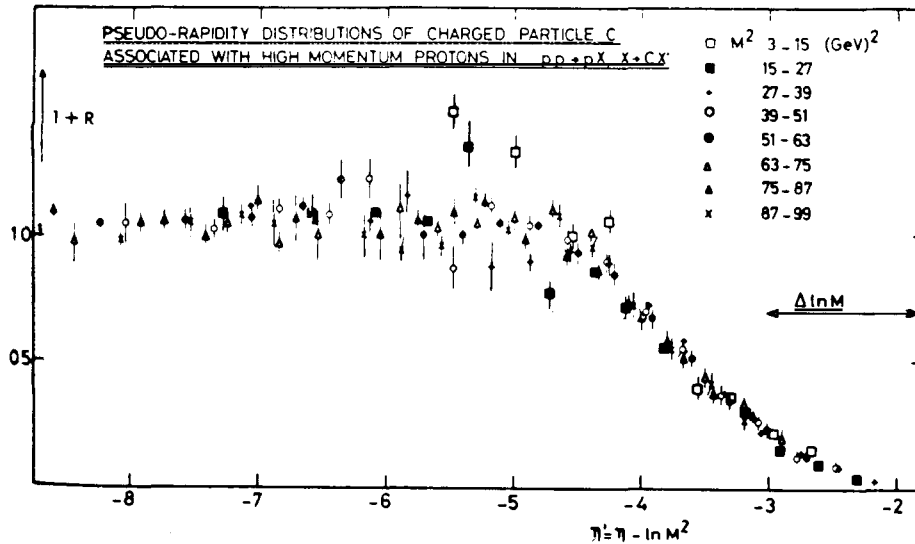
Fig. 36. The M^2 dependence of the pseudo-rapidity distribution of charged particles C produced in pp → pX, X → CX'. The vertical axis represents the pseudo-rapidity distribution, $dn_c/d\eta$, normalized to the single particle inclusive distribution, $(d\sigma/d\eta)/\sigma_{\text{inel}}$. The variable along the horizontal axis is $\eta' = \eta - \ln M^2$ ($m_p = 1$). The interval $\Delta \ln M$ represents the expected separation between the highest and lowest M^2 data for an η distribution of constant width (from ref. [46]).
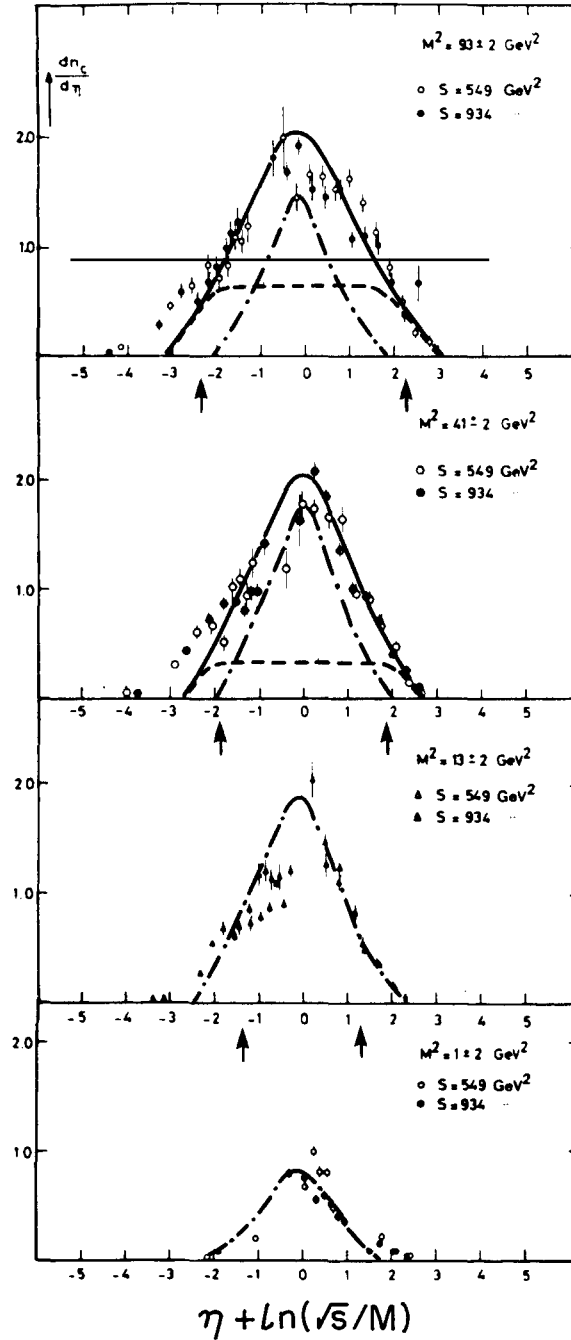
Fig. 37. Pseudo-rapidity distributions for charged particles C produced in pp→pX, X→CX' (from ref. [46]). The choice of variable along the horizontal axis is such that the distributions are expected to be centered at zero (see text, eq. (51)). The arrows below the horizontal axis of each figure point to the edges expected for multiperipheral type distributions. The broken curves represent multiperipheral distributions while the broken-dotted curves are of the isotropic fireball type. The ratio of the areas under two types of curves has been chosen to be equal to the amount of non-diffractive to diffractive events contained in the inclusive spectrum of each M^2. This ratio is about 1.5 and 0.3 for $M^2 = 93$ and 41 GeV^2, respectively, and negligible for the two lower values of M^2. The solid curves through the data are the sum of the above two distributions.

separated by $\ln(M_x/m_p)^2$ as expected by the multiperipheral model. While this result seems to provide strong support for this model, the contradiction with the Pisa–Stony Brook experiment must be reconciled before a conclusion can be drawn favoring one of the models.

As discussed in section 3.1 (eq. (43)), the inclusive recoil spectrum, $d\sigma/dx$, consists of two terms: a factorizable term that has a $1/(1-x)$ dependence and is identified as diffractive and a non-factorizable, presumably non-diffractive term, that goes as $(1-x)$. The ratio of the non-diffractive to the diffractive cross sections grows with $(1-x)$ and is approximately equal to $100\ (1-x)^2$; at $1-x = 0.1$ this ratio is unity while at $1-x = 0.03$ it is 0.1 (see eq. (43) and fig. 35b). Thus, the high mass region of the inclusive recoil spectrum is contaminated heavily by non-diffractive events. Let us now assume that the diffractive clusters are of the fireball type while the non-diffractive ones, belonging to the second term of eq. (43), are multiperipheral. The pseudo-rapidity distributions should then be described by a sum of fireball and multiperipheral type distributions in proportion, respectively, to the number of diffractive and non-diffractive events in the sample. Figure 37 shows CHLM clusters of different values of M_x^2 fitted by this procedure. With the exception of a small excess of events at the "outer" edges of the distributions, the fits are satisfactory. Thus, the CHLM data are compatible with the hypothesis that diffractive states decay isotropically, provided one assumes that the non-diffractive "background" is multiperipheral. It is also seen from fig. 37 that the widths of the overall distributions are much closer to the isotropic fireball width than to the multiperipheral widths defined by the arrow heads on the horizontal axis. This explains why the interpretation of the Pisa–Stony Brook data, which is based on the width rather than the edges of the pseudo-rapidity distributions, favors the fireball model.

The argument presented above does not, of course, constitute a direct proof of isotropy. Such proof can only be obtained at very high energies where large diffractive masses can be obtained free of background. The energies of the $\bar{p}p$ Colliders at CERN ($\sqrt{s} = 540\ \text{GeV}$) and at Fermilab ($\sqrt{s} = 2000\ \text{GeV}$) are adequately high for this purpose and an experiment to perform such a study at the Fermilab Collider has already been proposed [41].

An important consequence of isotropic decay is that the average transverse momentum of the fragments is expected to be higher for a diffractive mass M_x than for a central collision at $\sqrt{s} = M_x$. Naively, in the fireball model, the average p_T is

$$\langle p_T \rangle_{M_x} = \frac{\pi}{4} \frac{M_x}{1.5\langle n_c \rangle} \tag{54}$$

where $\langle n_c \rangle$ is the average charged multiplicity given by eq. (48) and the factor of 1.5 is introduced to account for π^0 production. Since the multiplicity increases only logarithmically with M_x, the average p_T of the fragment becomes larger as M_x increases. Assuming an $1/M_x^2$ dependence with a cut-off at $M_x^2 \cong 0.1s$, the average diffractive p_T calculated using eq. (54) is 0.7 GeV/c for $\sqrt{s} = 60$ GeV (ISR) and 1.8 GeV/c for $\sqrt{s} = 540$ GeV (SPS Collider). Such an increase of the average diffractive p_T with s would cause the overall $\langle p_T \rangle$ of the inclusive pp → anything collisions to increase with s even if the $\langle p_T \rangle$ of the hard core collisions remained constant.

The p_T of secondaries from high mass diffractive states has never been measured. The only experimental information on this subject comes from the CCHK collaboration at the ISR [48]. This experiment finds that the diffractive peak seen in the x distribution of recoil protons obtained with a minimum bias trigger is heavily suppressed when the presence of a particle with $p_T > 1$ GeV/c is required in the hemisphere opposite to that of the recoil proton. While this result seems to contradict the conclusion arrived at previously on the basis of isotropy in the decay of diffractive states, the

acceptance of the apparatus is such that this apparent contradiction is actually not valid. In the hemisphere opposite to the recoil particle, the acceptance is limited to $9° < \theta < 21°$. Now, the average p_T of a diffractive cluster is a function of the mass and hence of the average polar angle of the secondaries of the cluster. From eqs. (50), (51), (54) and (46b), one obtains

$$\bar{p}_T = \tfrac{1}{4} s^{1/4} (\tan(\bar{\theta}/2))^{1/2} \tag{55}$$

which for $\sqrt{s} = 52.5$ GeV and $9° < \bar{\theta} < 21°$ yields $0.51 < \bar{p}_T < 0.78$ GeV/c. Therefore, by excluding events with $p_T < 1$ GeV/c, the trigger is expected to eliminate most of the diffractive events, as is observed experimentally. Although this result does not constitute proof of eq. (54) and the underlying hypothesis of isotropy, these considerations show that it does not contradict it either. A measurement of the average p_T of diffractive clusters as a function of M_x is still in order.

Recently, an increase of the average p_T from ISR to SPS Collider energies was observed albeit indirectly. Experiment UA5 reported [49] that their pseudo-rapidity distribution at $\sqrt{s} = 540$ GeV could be fitted well by a model employing cylindrical phase space with $\langle p_T \rangle \cong 500$ MeV/c while in fitting ISR data at $\sqrt{s} = 53$ GeV, the same model required $\langle p_T \rangle = 350$ MeV/c. At ISR, the total single and double diffractive cross section, $\sigma_{in} - \sigma_0$, is about 10 mb (see fig. 41), while at the SPS Collider the double diffractive cross section, which is the only diffractive part contained in the UA5 data, is estimated to be about 7 mb (see section 4). In both cases, the hard core cross section is presumed to be the same, $\sigma_0 = 26.3$ mb. Assuming a fixed $\langle p_T \rangle$ for the hard core and the values of $\langle p_T \rangle$ given above for diffraction, a straightforward weighing of the $\langle p_T \rangle$ by the corresponding cross section gives $\langle p_T \rangle$ (hard core) = 300 MeV/c for the ISR data and, using this value, $\langle p_T \rangle$ (overall) = 495 MeV/c for the collider data with single diffraction excluded, in good agreement with the experimental value of 500 MeV/c. While this estimate is somewhat conjectural, it does indicate the need for studying separately the various components of the inelastic cross section.

4. Total cross section

At high energies, the difference between particle and antiparticle cross sections approaches zero approximately as $1/\sqrt{s}$ (fig. 38, ref. [3]) while all cross sections rise with s logarithmically. This behavior is expected by the critical pomeron Reggeon field theory [50]. Quantitatively, the predictions of this theory for pp and p̄p cross sections are compared [50] to a dispersion relations extrapolation of the ISR data [10] in fig. 39. While the dispersion analysis seems to predict higher cross sections, it is noted that this prediction depends on the extrapolation of the measured ρ-values to higher energies and is somewhat subjective (see fig. 17).

The critical pomeron prediction is shown [50] against cosmic ray data in fig. 40. The effective $\ln p$ dependence of this cross section, which is in agreement with the cosmic ray data, deviates substantially at SPS and Fermilab Collider energies from the $(\ln p)^2$ extrapolation [10] of the ISR data. However, as shown in fig. 41, the ISR cross sections are compatible with the expression $\sigma_T = 3.33\ (b_{el}) = 26.3 + 2.33 \ln p$, where $b_{el} = 7.9 + 0.7 \ln p$ represents the pp elastic slope parameter data at energies above ~ 100 GeV (see section 2.1.1 and fig. 10a). When this expression for σ_T, which at ISR energies satisfies geometrical scaling, is extrapolated to higher energies, it agrees well with the critical pomeron prediction.
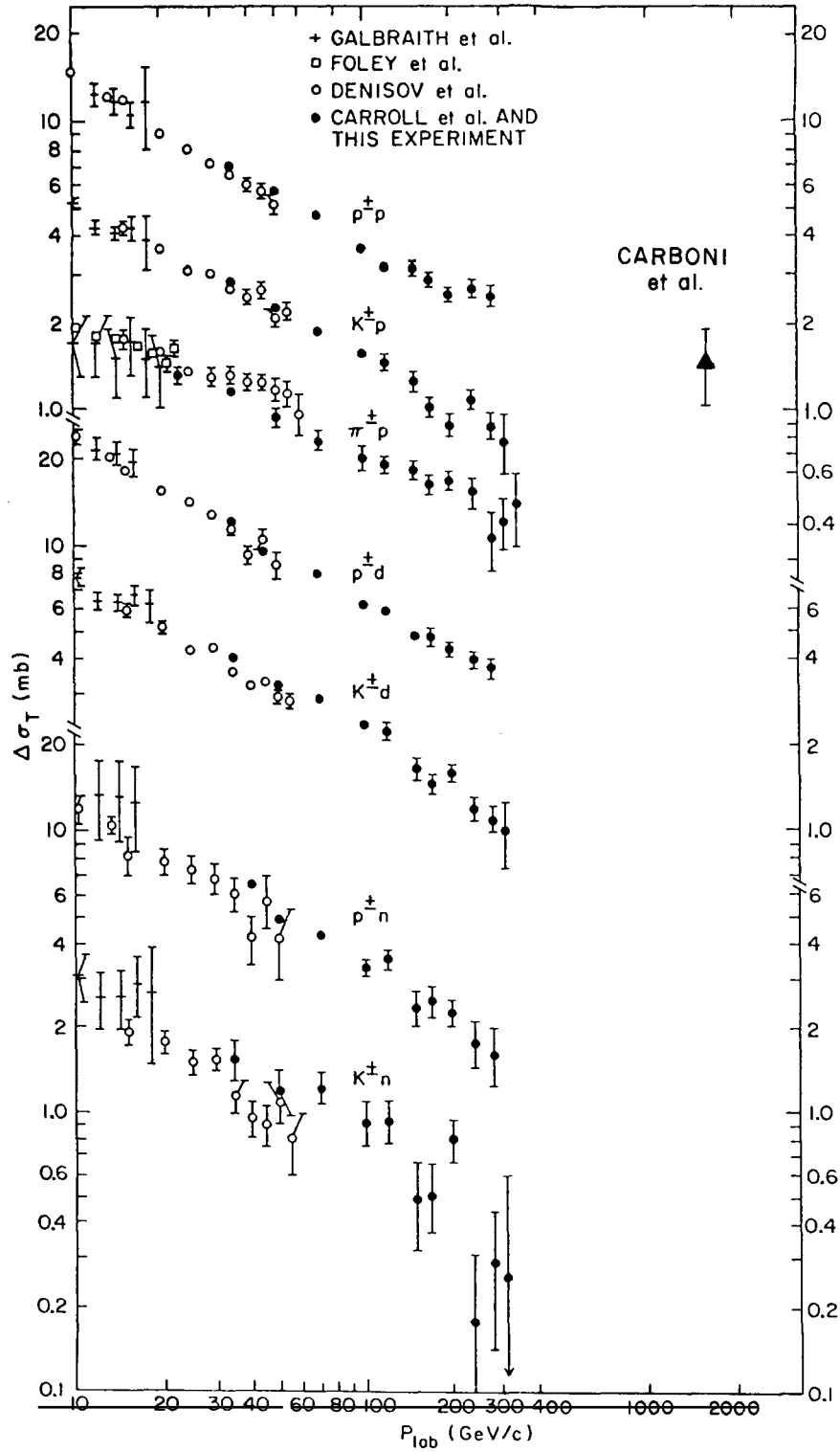
Fig. 38. Particle–antiparticle total cross section differences as a function of laboratory momentum (from ref. [3]).

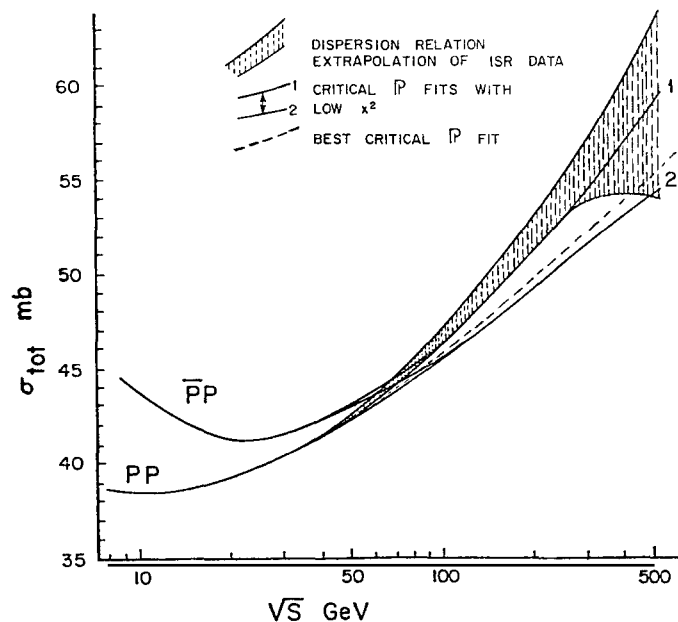Fig. 39. Critical pomeron predictions of pp and p̄p total cross sections at collider energies, compared to a dispersion relations extrapolation of the ISR data (from ref. [50]).
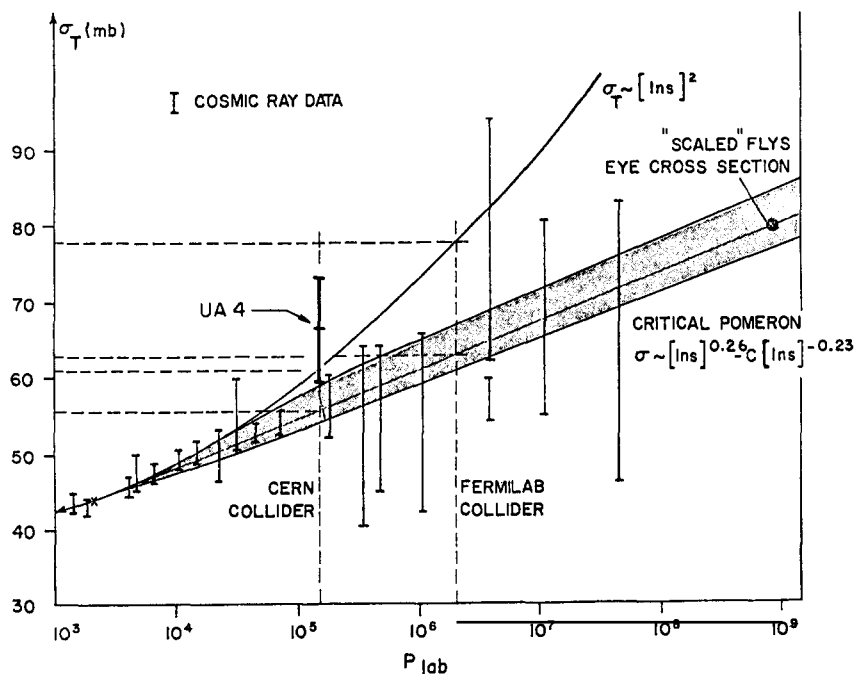

Fig. 40. Proton–proton total cross section as a function of laboratory momentum: Critical pomeron prediction compared with cosmic ray data and with a $(\ln s)^2$ extrapolation of the ISR data (from ref. [50]).
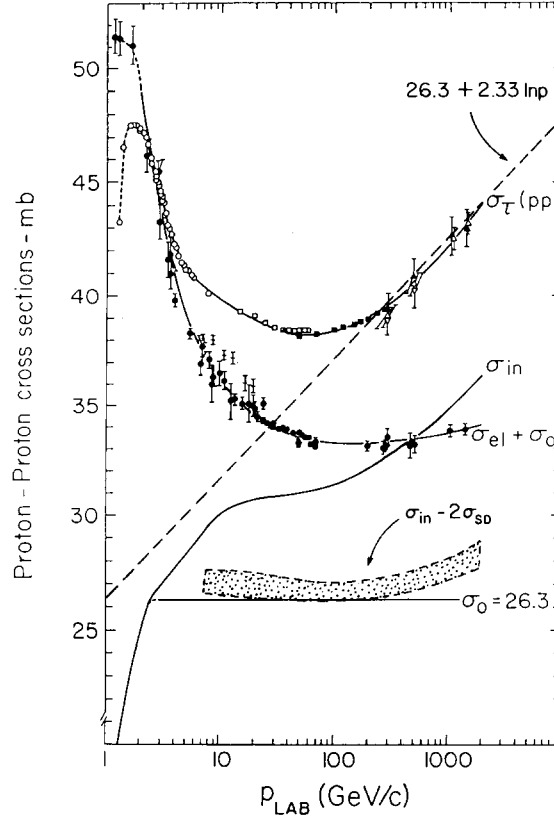
Fig. 41. Proton–proton cross sections as a function of laboratory momentum (see fig. 13a). After subtraction of twice the single diffraction dissociation cross section, as given by eq. (45), the remaining rise of the inelastic cross section with energy is small and consistent with the expected contribution from double diffraction dissociation (see text and fig. 42).

The question of how much of the rise of the pp inelastic cross section comes from diffraction dissociation is addressed in figs. 41 and 42. The total and inelastic cross sections shown in fig. 41 are the same as those in fig. 13a. The dotted band represents the inelastic cross section after subtraction of twice the value of the single diffraction dissociation cross section given by eq. (45). The quantity $\sigma_{in} - 2\sigma_{SD}$ still increases with energy, indicating that single diffraction dissociation alone cannot account for the rise of the inelastic cross section. This conclusion, stated explicitly in ref. [32], which reports the results of an ISR experiment in the energy range $549 < s < 1464$ GeV^2, has also been reached by a more recent ISR experiment [51] which measured σ_{SD} in the larger energy range of $550 < s < 3880$ GeV^2 or $290 < p_{lab} < 2060$ GeV/c. Quantitatively, the results of both these experiments, after correcting for the non-diffractive contribution as estimated by evaluating the integral of the second term of eq. (43), are in general agreement with the values of σ_{SD} given by eq. (45) and used in plotting the dotted band in fig. 41. In the range $200 < p_{lab} < 2000$ GeV/c, the rise of $\sigma_{in} - 2\sigma_{SD}$ exhibited by this band is about 2 mb. Some of this rise could, of course, be due to the rise of the cross section of the hard core. However, as shown below, it is quite possible that the entire rise of $\sigma_{in} - 2\sigma_{SD}$ may be due to the contribution of double diffraction dissociation, in which case the rise of σ_{in} with energy would be entirely diffractive.

Inclusive high mass double diffraction dissociation has never been measured. Using factorization, the
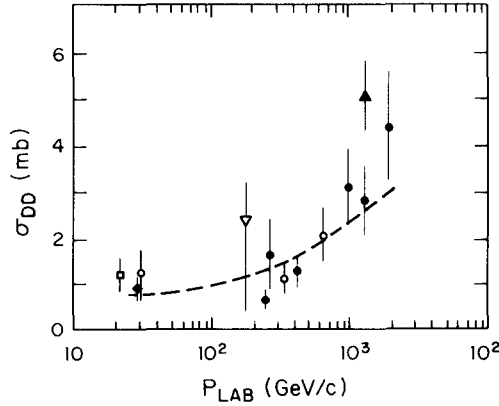
Fig. 42. The inclusive pp double diffraction dissociation cross section as a function of laboratory momentum. The data are from exclusive and semi-inclusive cross sections, such as $pp \to (p\pi^+\pi^-)(p\pi^+\pi^-)$ and $pp \to (p\pi^+\pi^-) + X$, scaled by the "branching fraction" $\sigma_{SD}(p \to p_D \to \text{all})/(\sigma_{SD} \to p_D \to p\pi^+\pi^-)$ (from ref. [52]). The curve was obtained using eq. (57) with $k = 4/3$, with σ_{SD} from eq. (45), and with σ_{el} from fig. 41.

cross section for $p + p \to X_1 + X_2$ is calculated to be [47]

$$\frac{d^3\sigma_{DD}}{dt\,dM_1^2\,dM_2^2} = \frac{d^2\sigma_1}{dt\,dM_1^2}\frac{d^2\sigma_2}{dt\,dM_2^2} \bigg/ \frac{d\sigma_{el}}{dt}.$$ (56)

Assuming $\exp(bt)$ dependence for both single diffraction dissociation and elastic scattering, integration of eq. (56) yields

$$\sigma_{DD} = k\,\sigma_{SD}^2/\sigma_{el}\ ; \qquad k = \frac{r^2}{(2r-1)}\ ; \qquad r = b_{SD}/b_{el}\ .$$ (57)

For $r = \frac{2}{3}$, $k = \frac{4}{3}$ while for $r = \frac{1}{2}$, $k = \infty$. Because of the sensitivity of the coefficient k on the value of r, the calculation of σ_{DD} using eq. (57) has a large uncertainty. In principle, the ratio r could be a function of s. Taking $r = \frac{2}{3}$, a value consistent with experimental results at Fermilab and ISR, we obtain $\sigma_{DD} = 1.4\,\text{mb}$ and $2.8\,\text{mb}$ at 200 and 2000 GeV/c, respectively, corresponding to a rise of 1.4 mb between the two energies. This value is very close to the rise represented by the dotted band in fig. 41. The full calculation of σ_{DD} as a function of s, using eq. (57) with $r = \frac{2}{3}$ or $k = \frac{4}{3}$, is shown as a dashed curve in fig. 42. The points plotted in this figure [4] represent fully inclusive double diffraction dissociation cross sections obtained from exclusive and semi-inclusive data, such as $pp \to (p\pi^+\pi^-)(p\pi^+\pi^-)$ and $pp \to (p\pi^+\pi^-) + X$, scaled by the "branching fraction" $[\sigma_{SD}(p \to p_D \to \text{all})/(\sigma_{SD} \to p_D \to p\pi^+\pi^-)]$. Also included in this figure are points obtained from data on $pK^\pm \to$ exclusive/semi-inclusive channels, reduced to pp cross sections using factorization [52]. It is evident, from fig. 42, that the double diffraction dissociation cross section is represented well by eq. (57) with $k = \frac{4}{3}$ and, by comparing figs. 41 and 42, that the rise of σ_{DD} with energy is sufficient to explain the entire rise of $\sigma_{in} - 2\sigma_{SD}$. Thus, when the contribution of all diffractive processes (elastic scattering, single and double diffraction dissociation) is subtracted from the total cross section, the non-diffractive "hard core" remains flat up to the highest ISR energy $\sqrt{s} \sim 60$ GeV). This conclusion justifies our writing the inelastic cross section in eq. (30) as $\sigma_{in}(s) = \sigma_0 + \sigma_D(s)$.

With a hard core cross section independent of s, the energy dependence of the total cross section is determined by the diffractive components. Assuming that the elastic and single diffractive cross sections are given, respectively, by eqs. (41) and (45) while double diffraction is given by eq. (57) with $k = \frac{4}{3}$, the s-dependence of the total cross section is completely determined by the equations:

$$\sigma_T = \sigma_0 + \sigma_{el} + 2\sigma_{SD} + \sigma_{DD} \tag{58}$$

$$\sigma_0 = 26.3 \text{ mb}$$

$$\sigma_{el} = 0.175\sigma_T + 0.825 \frac{35 \text{ (GeV}/c)}{p_{lab}} \qquad \text{[from eq. (41)]}$$

$$\sigma_{SD} = (0.68 \pm 0.05)\left(1 + \frac{36 \pm 8}{s}\right)\ln(0.6 + 0.1s) \qquad \text{[from eq. (45)]}$$

$$\sigma_{DD} = \frac{4}{3}\sigma_{SD}^2/\sigma_{el} .$$

In fig. 40, the solution of eqs. (58) for $\sigma_T(s)$ coincides with the critical pomeron prediction which passes through the "scaled flys-eye cross section". At lower energies, in the range of laboratory momenta from 2 to 2000 GeV/c, this solution lies within ~ 1 mb or $\sim 2\%$ of the experimental data. At $\sqrt{s} = 540$ GeV, it yields $\sigma_{SD} = 7.0$ mb, $\sigma_{el} = 10.0$ mb, $\sigma_{DD} = 6.5$ mb, and $\sigma_T = 57$ mb. The measured value of σ_T at $\sqrt{s} = 540$ GeV is [20] 66 ± 7 mb. However, the quoted error in this measurement is only statistical and systematic errors are expected to increase it. Thus, the measurement is not accurate enough to either confirm or contradict the prediction of eqs. (58). In any case, as mentioned earlier, inclusive double diffraction dissociation has not yet been measured directly. In light of the success of eqs. (58) at energies below $\sqrt{s} = 60$ GeV, a measurement of σ_{DD} along with σ_{SD}, σ_{el} and σ_T at collider energies may indeed provide the answer to the question of rising cross sections.

5. Elastic and total cross sections – Are they related through diffraction dissociation?

In section 3.2 it was shown that the high mass diffractive cross sections of hadrons interacting with protons scale as the corresponding total cross sections. Later, in section 3.3, it was argued that the integrals over t of the low mass diffractive cross sections should also scale as the total cross sections. Our argument was based on the fact that these integrals follow the $1/M_x^2$ law and have the same s-dependence throughout the entire M_x^2 region, including the low mass enhancements (see fig. 22c and section 3.1). This behavior suggests that low mass and high mass diffraction are similar in character and therefore, it is reasonable that they should obey the same factorization rules. Using the FMSR, eq. (14), we then obtain the relationship

$$\sigma_T \sim \int_0^\infty |t|(d\sigma_{el}/dt)\,dt = \sigma_{el}/b_{el} ,$$

where in deriving the last step we assumed the form $\exp(b_{el}t)$ for $d\sigma_{el}/dt$. From the optical theorem, on

the other hand, we obtain $d\sigma_{el}/dt = (\sigma_T^2/16\pi)\exp(b_{el}t)$ or $\sigma_{el} \sim \sigma_T^2/b_{el}$, assuming $\rho = 0$, which is a good approximation at high energies. Thus, $\sigma_T \sim \sigma_{el}/b_{el} \sim \sigma_T^2/b_{el}^2$. This leads to $b_{el}/\sigma_T^{1/2} = c'(s)$ and $\sigma_{el}/\sigma_T^{3/2} = c(s)$, where $c'(s)$ and $c(s)$ are the same for all hadrons. These relationships were compared to data in sections 2.1.1 and 2.3 and were found to hold remarkably well (see figs. 15 and 18).

The s-dependence of the diffractive cross section can now be understood in terms of that of elastic scattering. Since the integral over t of $d^2\sigma/dt\,dM_x^2$ behaves as $1/M_x^2$ and has the same s-dependence throughout the entire M_x^2 region, the FMSR yields

$$d\sigma/dM_x^2 \sim (1/M_x^2) \int_0^\infty |t|(d\sigma_{el}/dt)\,dt.$$

Using eq. (40) for $d\sigma_{el}/dt$ with $r = 0.217$ (value at 200 GeV; r is approximately constant over the Fermilab energy range) we obtain $d\sigma/dM_x^2 \sim (1/M_x^2)(1 + 35/s)$ and therefore $\sigma_{SD}(pp \to Xp) = A(1 + 35/s)\ln(0.6 + 0.1s)$. The s-dependence of this equation is in excellent agreement with eq. (45) which represents the experimental data.

We have seen above that the elastic and diffractive cross sections of protons incident on protons are related through the FMSR. Presumably, this is also the case for all other hadrons. On the other hand, the diffractive cross sections for $hp \to Xp$ are related to the corresponding total cross sections, $hp \to$ anything, through factorization. Thus, diffraction dissociation links the elastic cross sections of different hadrons interacting with protons to the corresponding total cross sections. The resulting relationship, $\sigma_{el}/\sigma_T^{3/2} =$ constant for all hadrons at the same s, is difficult to understand in terms of any other model. Since it was derived under the assumption that the amplitude responsible for low mass diffraction is of the same character as that for high mass diffraction (triple-pomeron), the fact that it holds experimentally is evidence that this is indeed the case.

6. Diffraction at the p̄p Colliders

The importance of high energies for hadronic diffraction has been emphasized throughout this article. The CERN p̄p Collider with $\sqrt{s} = 540$ GeV and the forthcoming Fermilab Collider with $\sqrt{s} = 2000$ GeV provide excellent tools for the study of diffractive interactions. Total cross sections and elastic scattering can be measured using the techniques developed at the ISR. Such measurements have already been performed at CERN, but the statistical and systematic uncertainties are still large; better measurements are needed. The recoil technique, which has been used successfully at lower energies for the measurement of the mass in single diffraction dissociation, is not accurate enough at the energies of the Colliders. The method of obtaining the mass from the average pseudo-rapidity of the secondaries seems more promising. An added advantage of this method is that it can also be applied to inclusive double diffraction dissociation. A proposal to study single and double diffraction dissociation using this technique has been submitted to Fermilab [41].

From a purely phenomenological point of view, the discussion in this paper suggests that measurements to be performed and questions to be answered at the Colliders should include:

(i) *Total cross sections* –
From a measurement of the total cross section and of its diffractive components, one may obtain the

ratio σ_{el}/σ_T and the cross section of the "hard core", $\sigma_0 = \sigma_T - \sigma_{el} - 2\sigma_{SD} - \sigma_{DD}$. At ISR energies, $\sigma_{el}/\sigma_T = 0.175$ (eq. (41)) and $\sigma_0 = 26.3$ mb, independent of s (eq. (58)). Geometrical scaling predicts that σ_{el}/σ_T should still be the same at Collider energies while the critical pomeron Reggeon field theory predicts that, if it changed at all, σ_{el}/σ_T should become smaller. As for the hard core cross section, all theories expect that it should grow with s. The fact that it has remained constant throughout the entire energy region from threshold to $\sqrt{s} = 60$ GeV (see section 4) is puzzling. It would be interesting to check whether σ_0 will maintain the same value at Collider energies. To this end, the direct measurement of inclusive double diffraction dissociation is crucial.

(ii) Elastic scattering –

In addition to the total elastic cross section, the measurement of the differential cross section is also important. The small t behavior of $d\sigma_{el}/dt$ at lower energies has been discussed extensively in this paper. We still lack a theoretical understanding of the s and t dependence of the slope parameter at low t and measurements at Collider energies may help clarify the situation. Of course, high t elastic scattering is also interesting as discussed in ref. [4].

(iii) Single and double diffractive differential cross sections –

Does the triple-pomeron amplitude of the Regge model, which provides a good description at lower energies, continue to do so at the energies of the Colliders? According to this model, as the energy increases and all diffractive masses move to smaller values of $1 - x = M_x^2/s$, larger masses become incorporated into the diffraction region $(1 - x \leq 0.1)$. This results in an increase of the total diffractive cross section which, as discussed in section 4, may very well be solely responsible for the increase of the inelastic cross section with energy (when both single and double diffraction dissociation are taken into account).

As a given M_x^2 moves to lower values of $1 - x$, the associated non-diffractive "background" becomes smaller (eq. (43)). Therefore, a larger mass range becomes available for the study of diffractive cross sections, charged multiplicities and decay distributions. An additional advantage of high energies is that the separation of the pseudo-rapidity clusters of two given masses in double diffraction dissociation increases with s, facilitating further the study of double diffraction at the $\bar{p}p$ Colliders.

(iv) Charged multiplicity distributions –

The need for measuring separately the charged multiplicity distribution of each individual component of the inelastic cross section (hard core, single and double diffraction dissociation) was discussed extensively in section 3.5. At energies up to $\sqrt{s} \cong 60$ GeV, the multiplicities for pp→anything are described well by a Gaussian function of the available mass (see eq. (46)). However, a direct test of this function against diffractive multiplicities has been performed only for masses up to 6 GeV [35]. At $\sqrt{s} = 540$ and 2000 GeV, where diffractive masses as large as about 150 and 600 GeV are expected to be excited, the study of the diffractive and hard core multiplicity distributions will undoubtedly provide us with a clearer picture of the phenomenology and a better understanding of the KNO scaling behavior.

(v) Decay distributions –

With large diffractive masses at small values of $1 - x$ where the non-diffractive background is negligible, it should now be easier to discriminate between the isotropic fireball type and the multiperipheral type models of diffraction dissociation. At higher values of $1 - x$, the background is larger but so are the masses and the corresponding charged multiplicities. With more particles in the

final state it may now be statistically possible to separate the diffractive from the non-diffractive clusters on an event by event basis if they belong, respectively, to the fireball and the multiperipheral type distributions as discussed in section 3.6. If such a separation could be performed, the $1/M_x^2$ behavior of diffraction dissociation could be followed to values of $1 - x$ larger than the usual $\sim$0.1, up to the cut-off imposed by t_{min}.

Finally, the measurement of the transverse momentum distribution of the diffractive clusters at the Colliders may provide an answer to the question of rising $\langle p_T \rangle$ and solve the puzzle of large transverse momentum events observed in cosmic rays [53].

Acknowledgments

References

[1] D.R.O. Morrison, CERN Preprint D.Ph.II/Phys 73-46.
[2] K. Goulianos, Proc. XIIIth Rencontre de Moriond, Vol. I (1978) pp. 457–469.
[3] S. Carroll et al., Phys. Lett. 80B (1979) 423;
    G. Carboni et al., Phys. Lett. 113B (1982) 87.
[4] G. Alberi and G. Goggi, Phys. Reports 74, No. 1 (1981) 1–207.
[5] J. Dias de Deus, Nucl. Phys. B59 (1973) 231;
    A.J. Buras and J. Dias de Deus, Nucl. Phys. B71 (1974) 481.
[6] A.I. Sanda, Phys. Rev. D6 (1972) 280;
    M.B. Einhorn, J. Ellis and J. Finkelstein, Phys. Rev. D5 (1972) 2063.
[7] D.P. Roy and R.G. Roberts, Nucl. Phys. B77 (1974) 240;
    R.D. Field and G.C. Fox, Nucl. Phys. B80 (1974) 367.
[8] L.N. Hand et al., Rev. Mod. Phys. 35 (1963) 335;
    A. Quenzer et al., Phys. Lett. 76B (1978) 512 and references therein;
    E. Dally et al., XIX Intern. Conf. on High Energy Physics, Tokyo, August 1978.
[9] B. West and D.R. Yennie, Phys. Rev. 172 (1968) 1413.
[10] U. Amaldi et al., Phys. Lett. 66B (1977) 390.
[11] U. Amaldi et al., Phys. Lett. 36B (1971) 400;
    G. Barbiellini et al., Phys. Lett. 39B (1972) 663;
    G.G. Beznogikh et al., Phys. Lett. 43B (1973) 85;
    V. Bartenev et al., Phys. Rev. Lett. 31 (1973) 1088;
    U. Amaldi et al., Phys. Lett. 44B (1973) 116; 66B (1977) 390;
    L. Baksay et al., Nucl. Phys. B141 (1978) 1.
[12] D.S. Ayres et al., Phys. Rev. D15 (1977) 3105;
    J.P. Burq et al., Phys. Lett. 77B (1978) 438;
    A. Schiz et al., Phys. Rev. D24 (1981) 26;
    R.L. Cool et al., Phys. Rev. D24 (1981) 2821;
    J.P. Burq et al., Phys. Lett. 109B (1982) 111.
[13] J.P. Burq et al., Intern. Conf. on High Energy Physics, July 1981, Lisbon, Portugal.
[14] A. Schiz et al., Phys. Rev. D24 (1981) 26.
[15] A.A. Anselm and V.N. Gribov, Phys. Lett. 40B (1972) 487;
    J.W. Alcock et al., Nucl. Phys. B67 (1973) 445;
    J. Pumplin et al., Phys. Rev. D10 (1974) 2918.
[16] K. Goulianos, Phys. Rev. D14 (1976) 1445.

[17] A. Capella and M.S. Chen, Phys. Rev. D8 (1973) 2097;
     N.I. Starkov and V. Tsarev, Pisma Zh. E.T.F. 23 (1976) 403 [JETP Lett. 23 (1976) 363].
[18] R. Battiston et al. [UA-4 Collaboration], Phys. Lett. 115B (1982) 333.
[19] G. Arnison et al. [UA-1 Collaboration], Phys. Lett. 121B (1983) 77.
[20] R. Battiston et al. [UA-4 Collaboration], Phys. Lett. 117B (1982) 126.
[21] L.A. Fajardo et al., Phys. Rev. D24 (1981) 46.
[22] W.F. Baker et al., Phys. Rev. Lett. 47 (1981) 1683.
[23] Y. Akimov et al., Phys. Rev. Lett. 35 (1975) 763.
[24] Y. Akimov et al., Phys. Rev. Lett. 35 (1975) 766.
[25] Y. Akimov et al., Phys. Rev. D14 (1976) 3148.
[26] D.S. Ayres et al., Phys. Rev. Lett. 37 (1976) 1724.
[27] R.L. Anderson et al., Phys. Rev. Lett. 38 (1977) 880.
[28] Y. Akimov et al., Phys. Rev. Lett. 39 (1977) 1432;
     D.F. Nitz, Ph.D. Thesis, University of Rochester, Department of Physics and Astronomy, Rochester, NY.
[29] R.D. Schamberger et al., Phys. Rev. D17 (1978) 1268.
[30] E. Jenkins et al., FERMILAB – Pub-79/56 – EXP.
[31] R.L. Cool et al., Phys. Rev. Lett. 47 (1981) 701.
[32] M.G. Albrow et al., Nucl. Phys. B108 (1976) 1.
[33] A. Capella, H. Hogaasen and V. Rittenberg, Phys. Rev. D8 (1973) 2040.
[34] Y. Antipov et al., Nucl. Phys. B63 (1973) 141.
[35] R.L. Cool et al., Phys. Rev. Lett. 48 (1982) 1451.
[36] Z. Koba, H.B. Nielson and P. Olesen, Nucl. Phys. B40 (1972) 317.
[37] K. Goulianos et al., Phys. Rev. Lett. 48 (1982) 1454.
[38] K. Goulianos, AIP Conf. Proc. No. 85, Proton–Antiproton Collider Physics, 1981, Madison, Wisconsin, eds. V. Barger, D. Cline, F. Halzen (American Institute of Physics, New York, 1982) pp. 469–485.
[39] K. Alpgard et al. [UA-5 Collaboration], Phys. Lett. 121B (1983) 209.
[40] G. Arnison et al. [UA-1 Collaboration], Phys. Lett. 107B (1981) 320.
[41] T. Chapin et al., A Proposal to Measure Single and Double Diffraction Dissociation at the FERMILAB p̄p Collider, The Rockefeller University, New York, NY 10021 (FERMILAB proposal P-725).
[42] R. Hwa, Phys. Rev. Lett. 26 (1971) 1143;
     M. Jacob and R. Slansky, Phys. Rev. D5 (1972) 1847.
[43] D. Amati et al., Nuovo Cimento 26 (1962) 896;
     G.C. Fox, Inclusive structure of diffraction scattering, CALT-68-413.
[44] E.L. Berger, Phys. Lett. 43B (1973) 132.
[45] G. Bellettini, AIP Conf. Proc. No. 15, High Energy Collisions, 1973 (Stony Brook), ed. Chris Quigg (American Institute of Physics, New York, 1973) pp. 9–46.
[46] M.G. Albrow et al., Phys. Lett. 51B (1974) 424;
     M.G. Albrow et al., Nucl. Phys. B102 (1976) 275.
[47] K. Goulianos, Diffractive Jets, Proc. Europhysics Study Conf. (Jet Structure from Quark and Lepton Interactions), Erice-Trapani-Sicily, September 1982.
[48] M. Della Negra et al., Phys. Lett. 59B (1975) 401.
[49] K. Alpgard et al. [UA-5 Collaboration], Phys. Lett. 107B (1981) 310.
[50] A. White, AIP Conf. Proc. No. 85, Proton–Antiproton Collider Physics, 1981, Madison, Wisconsin, eds. V. Barger, D. Cline, F. Halzen (American Institute of Physics, New York, 1982) pp. 363–434.
[51] J. Armitage et al., Nucl. Phys. B194 (1982) 365.
[52] A. Givernaud et al., Nucl. Phys. B152 (1979) 189.
[53] C.M.G. Lattes et al., Physics Reports 65, No. 3 (1980) 151–229.